



HAL
open science

Vertical Deformation Along a Strike-Slip Plate Boundary: The Uplifted Marine Terraces of the Gulf of Aqaba and Tiran Island, at the Southern End of the Dead Sea Fault

Matthieu Ribot, Marthe Lefèvre, Yann Klinger, Edwige Pons-branchu, Arnaud Dapoigny, Sigurjón Jónsson

► To cite this version:

Matthieu Ribot, Marthe Lefèvre, Yann Klinger, Edwige Pons-branchu, Arnaud Dapoigny, et al.. Vertical Deformation Along a Strike-Slip Plate Boundary: The Uplifted Marine Terraces of the Gulf of Aqaba and Tiran Island, at the Southern End of the Dead Sea Fault. *Tectonics*, 2024, 43 (9), 10.1029/2023tc007977 . hal-04692226

HAL Id: hal-04692226

<https://hal.science/hal-04692226>

Submitted on 9 Sep 2024

HAL is a multi-disciplinary open access archive for the deposit and dissemination of scientific research documents, whether they are published or not. The documents may come from teaching and research institutions in France or abroad, or from public or private research centers.

L'archive ouverte pluridisciplinaire **HAL**, est destinée au dépôt et à la diffusion de documents scientifiques de niveau recherche, publiés ou non, émanant des établissements d'enseignement et de recherche français ou étrangers, des laboratoires publics ou privés.

Key Points:

- Extension along the Dead Sea strike-slip Fault
- Uplift determination from fossil coral terraces
- Interplay between Dead Sea strike-slip and Red Sea spreading center

Supporting Information:

Supporting Information may be found in the online version of this article.

Correspondence to:

M. Ribot,
matthieu.ribot@kaust.edu.sa

Citation:

Ribot, M., Lefèvre, M., Klinger, Y., Pons-Branchu, E., Dapoigny, A., & Jónsson, S. (2024). Vertical deformation along a strike-slip plate boundary: The uplifted marine terraces of the Gulf of Aqaba and Tiran Island, at the southern end of the Dead Sea Fault. *Tectonics*, *43*, e2023TC007977. <https://doi.org/10.1029/2023TC007977>







Received 21 JUN 2023
Accepted 26 JUL 2024

© 2024. The Author(s).

This is an open access article under the terms of the [Creative Commons Attribution License](#), which permits use, distribution and reproduction in any medium, provided the original work is properly cited.



Vertical Deformation Along a Strike-Slip Plate Boundary: The Uplifted Marine Terraces of the Gulf of Aqaba and Tiran Island, at the Southern End of the Dead Sea Fault

Matthieu Ribot^{1,2,3} , Marthe Lefèvre² , Yann Klinger² , Edwige Pons-Branchu³ ,
Arnaud Dapoigny³ , and Sigurjón Jónsson¹ 

¹King Abdullah University of Science and Technology (KAUST), Thuwal, Saudi Arabia, ²Institut de Physique du Globe de Paris (IPGP), CNRS, Université de Paris Cité, Paris, France, ³Laboratoire des Sciences du Climat et de l'Environnement, LSCE/IPSL UMR CEA/CNRS/UVSQ, Université Paris Saclay, Gif-sur-Yvette, France

Abstract Close to its southern end where it connects to the Red Sea rift, the Dead Sea strike-slip fault (DSF) becomes trans-tensional in the Gulf of Aqaba. Details of this transition, however, remain difficult to unravel as most of the active tectonic structures are located off-shore. This study focuses on uplifted marine terraces located in the Gulf of Aqaba and on Tiran Island. Using high-resolution tri-stereo Pleiades satellite imagery, we build a Digital Surface Model (DSM) at a 0.5-m resolution of the eastern coast of the gulf and Tiran Island to map 19 levels of marine terraces. The terraces are preserved at elevations from 1 m to almost 500 m above the current sea level. Correlating laterally U-Th ages obtained along the gulf with the lower levels found on Tiran Island, we build an age model to estimate the ages of the upper terraces on the island. Combining this with the terrace heights from our DSM, we derive the uplift rate affecting the terraces. The geographic extent of the terraces along the gulf suggests that the DSF is responsible for uplift along the entire eastern coastline of the gulf at a rate of about 0.14 ± 0.03 mm/year at least over the Quaternary. The uplift rate of Tiran Island, located closer to the Red Sea rift, is faster at 0.21 ± 0.02 mm/year over the past 2.4 Myr. This faster uplift rate suggests a combined tectonic uplift related to both the Dead Sea strike-slip fault system and the Red Sea rift.

1. Introduction

Assessment of the vertical deformation along a strike-slip plate boundary is challenging as most of the deformation is accommodated by horizontal strike-slip motion, with usually minor vertical motion related to compressional or extensional deformation. When a strike-slip fault is perfectly aligned with the small circle defined by the Euler pole describing the relative plate motion, no vertical motion is expected. However, irregularities in the fault geometry (Garfunkel et al., 1981; Joffe & Garfunkel, 1987) or even changes in the regional stress field (Ben-Avraham & Zoback, 1992) might result in vertical motion along the faults, which can impact the finite deformation and imprint the landscape morphology on long timescales.

1.1. Geological Background

The history of the Dead Sea Fault (DSF) system is closely related to the development of the extensive Red Sea rift system located at its southern termination (Figure 1). During the Oligocene, in parallel with the closure of the great Tethys Ocean in the north, rifting in Afar (Hughes et al., 1991; Garfunkel & Beyth, 2006) and in the Gulf of Aden began (Davison et al., 1994; Hughes et al., 1991). This was followed (~24 Myr) by rifting of the Red Sea and Gulf of Suez toward the NW (Garfunkel et al., 1987; Joffe & Garfunkel, 1987) (Figure 1a). During the Miocene (23–5 Myr), it is established that the Red Sea rift was connected with the compressional system of the Taurus Mountains through the DSF (Freund et al., 1970; Garfunkel, 1981) (Figure 1a). However, the exact timing of the initiation of the DSF is still debated with two competing scenarios: One proposition sets a maximum limit between 20 Myr (Alamri et al., 1991; Lyberis, 1988), from the age of dikes aligned along the Egyptian and Saudi Arabian coasts and affected by the largest offset of the fault, and 17–18 Myr from to syn-sedimentary deposits in Lebanon (Elias, Tapponnier, Surssock, et al., 2007). On the other hand, following the ideas developed by several authors (Bosworth & Burke, 2005; Patton et al., 1994; Tubbs et al., 2014), Delaunay et al. (2023) have proposed a scenario involving a more recent initiation of the DSF, around 14 Myr, contemporaneous with the change in direction of the Red Sea extension, when the extension became more oblique to the rift and aligned along the same direction as of the current DSF (N20°E) (Badawy & Horváth, 1999; Khair et al., 1997; Le Pichon &

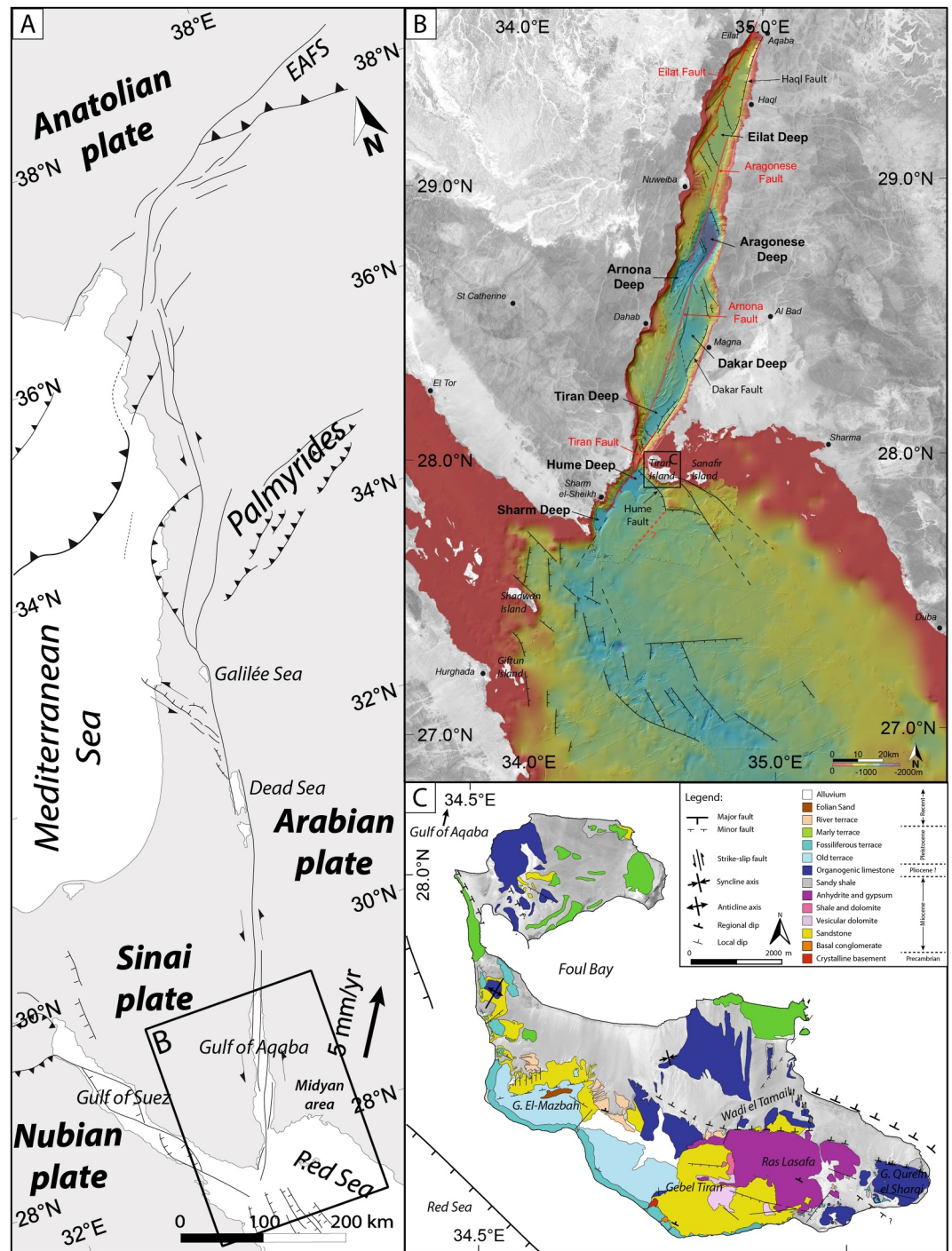


Figure 1. (a) Tectonic setting of the Dead Sea Fault (DSF) system, modified from Daëron et al. (2004), Elias, Tapponnier, Singh, et al. (2007), and Le Béon et al. (2008). (b) Bathymetric map of the northern Red Sea and Gulf of Aqaba combining R/V Thuwal (2018 (Ribot et al., 2021), 2019), SHOM (2004), and GMRT 3.7 (Ryan et al., 2009) data sets. Mapping of the faults in the northern Red Sea is modified from Courtillot et al. (1987) and Mart and Ross (1987). The red dashed line east of the Hume Deep and Sharm Deep corresponds to the possible last en-echelon strike-slip fault of the DSF. (c) Geological map of Tiran Island, modified from Goldberg and Beyth (1991) and adjusted on a high-resolution Pleiades Satellite imagery.

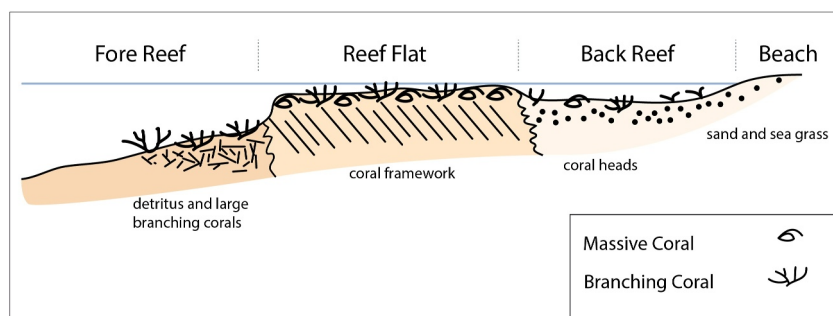


Figure 2. A schematic cross-section through a fossil fringing reef terrace of the type seen in the Gulf of Aqaba showing the three main reef zones. The blue line marks the inferred paleo-sea level. Modified from Bar et al. (2018).

Gaulier, 1988), leading to the development of the DSF along the western margin of the Arabian plate (Bayer et al., 1988).

The southern termination of the DSF, in the Gulf of Aqaba, is characterized by a large topography between the bottom of the Gulf of Aqaba, at 1,775 m bsl (Ben-Avraham et al., 1979; Ribot et al., 2021; Sade et al., 2009) and the mountain range that is bounding the gulf, peaking at 1,876 m asl. Part of this topographic relief is due to the recent extension along the southern end of the DSF and so is deemed to be less than 20 million years old, emphasizing the significance of the vertical deformation (Delaunay et al., 2023).

The horizontal left-lateral strike-slip motion of ~ 5 mm/year is well constrained since at least the mid-Pleistocene, based on geological markers (Bartov et al., 1980; Garfunkel et al., 1981; Goren et al., 2015; Klinger et al., 2000; Le Béon et al., 2010, 2012; Li et al., 2021; Niemi et al., 2001; Wechsler et al., 2018) and Global Positioning System (GPS) measurements (Al Tarazi et al., 2011; Castro-perdomo et al., 2022; Gomez et al., 2007; Hamiel et al., 2018; Le Béon et al., 2008; Masson et al., 2015; Pietrantonio et al., 2016; Reilinger et al., 2015; Sadeh et al., 2012; Viltres et al., 2022; Wdowski et al., 2004). The estimation of the vertical motion, however, is still debated as the deformation rate is small and thus, more difficult to ascertain (Bosworth et al., 2017; Gvirtzman et al., 1992; Lefevre, 2018).

In the region of the Gulf of Aqaba, the interaction between the Dead Sea strike-slip fault system and the extensive Red Sea spreading system leads to the formation of a complex fault zone with faults oriented $N20^{\circ}E$, along the main strike of the DSF, and faults oriented $N140^{\circ}E$, along the main axis of the Red Sea spreading (Figure 1). At the intersection of these two systems, Tiran Island is the last emerging marker of deformation at the termination of both systems on the Arabian Plate (Figure 1b).

Tiran Island covers a surface of ~ 63 km² and is composed of two main parts. The northern peninsula (~ 12 km²) is separated from the main southern part (~ 50 km²) by the Foul Bay. The two parts are connected by “the neck” (Schick, 1958). The Tiran block is made of Precambrian basement (Goldberg & Yaron, 1978), covered by thick layers of evaporites dating from the Mio-Pliocene (Figure 1c). Along its south-western side, several levels of coral terraces have been preserved (Goldberg & Beyth, 1991; Goldberg & Yaron, 1978; Schick, 1958).

1.2. Marine Terraces

Two main types of marine terraces can be distinguished: the marine terraces formed by the mechanical abrasion of the waves (see Anderson et al. (1999) and de Gelder et al. (2019)), and the marine terraces formed by bio-construction of living colonies (i.e., corals reef).

The terraces formed by bio-construction follow a typical reef structure (Figure 2) (Friedman, 1968; Gabrie & Montaggioni, 1982; Kennedy & Woodroffe, 2002; Mergner & Schuhmacher, 1974) that is from the beach: (a) the Back Reef, also named the lagoon, a zone that is protected from storms and wave energy, (b) the Reef Flat (RF), a zone that corresponds to the sea level at low tide, and (c) the Fore Reef (FR), a zone that generally consists of coarse debris coming from the erosion of the RF mixed with local well-developed living corals.

The reef platform is developing at an elevation corresponding to the Mean Sea Level (MSL) with the difference in elevation between the RF and the Beach depending on the amplitude of the tide. In addition, the variation in height

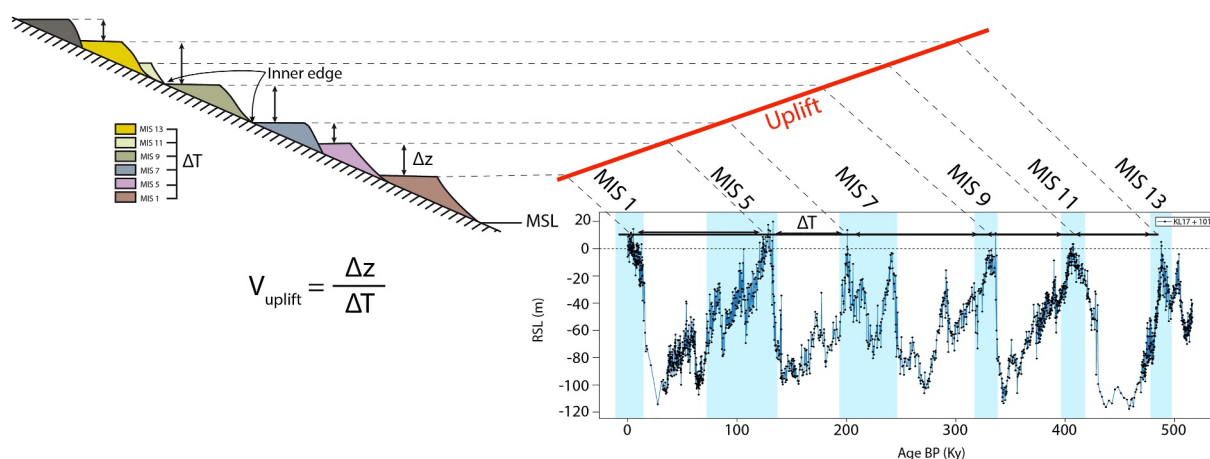


Figure 3. Reconstruction of the past sea level over the last 500 Kyr compiled from Rohling et al. (2009) with on the left a schematic view of uplifted reef terraces (modified from Woodroffe and Webster (2014)). The high stands identified represent the interglacial Marine Isotopic Stage (MIS). Coastal uplift rate V_{uplift} for the given time interval can be obtained from the elevation difference (Δz) and age difference (ΔT) between two terraces, MSL, Mean Sea Level; RSL, Relative Sea Level.

at the same site between the RF and the FR can be significant and reach locally several meters. In the Gulf of Aqaba and Strait of Tiran the average amplitude of tides is small, about 1 m (Friedman, 1968; Gvirtzman, 1994; Mergner & Schuhmacher, 1974; Shaked et al., 2005).

Marine terraces mostly develop when the sea level is stable. Thus, they are good recorders of the eustatic fluctuations over time (Figure 3) (Lisiecki & Raymo, 2005; Rohling et al., 2007, 2009, 2012; Siddall et al., 2003). The terraces are also used as a marker of the tectonic deformation and they have been used to quantify the tectonic uplift or subsidence due to the dip-slip motion on a fault located nearby, by comparing their current elevation with their initial position during formation (e.g., Indian Ocean, Hawaii, New Guinea, Gulf of Corinth, Gulf of Aqaba (Armijo et al., 1996; Bosworth et al., 2017; de Gelder et al., 2019, 2020; Husson et al., 2018; Manaa et al., 2016; Pedoja et al., 2011; Roberts et al., 2013; Woodroffe & Webster, 2014)). Due to the elastic nature of the crustal deformation, the vertical deformation at the fault decreases when one moves away from the fault. Hence, the uplift rate measured at a specific point along a marine terrace will depend on the distance between the terrace and the fault responsible for the deformation. Thus, marine terraces of similar ages, but located at a different distance from the fault responsible for deformation, will rest at different elevations (Armijo et al., 1996; Bott, 1997; de Gelder et al., 2019).

As defined by Armijo et al. (1996), the marine terraces have a landward margin, named inner edge (see Figure 3), marked by the shoreline angle, and a seaward margin marked by an eroded cliff. Along the Gulf of Aqaba and on Tiran island, the location of the inner edge of the terraces is not accessible due to colluvium deposits. One could project the location of the inner edge on a cross-section perpendicular to the paleo-shoreline, however, due to the limited geographical extent of the terraces, the virtual prolongation of the slope of the terrace would generate more uncertainties than considering the average elevation of each terrace as representative of the paleo elevation of the sea-level.

During the last 900 Kyr, glacial-interglacial cycles lasted about 70–120 Kyr, correlating with the major temperatures and sea-level variations. During the Early to Middle Pleistocene, however, the glacial-interglacial cycles were shorter, with periods of about ~30–60 Kyr (Figures 3 and 4) (Lisiecki & Raymo, 2005; Rohling et al., 2007; Siddall et al., 2003). During glacial periods, which correspond to sea-level low-stand periods, the MSL was about one hundred meters below the current MSL. Conversely, during interglacial periods, which correspond to sea-level high-stand periods, the MSL was close to the current MSL, within ± 10 m fluctuations.

Combining the quaternary eustatic variations with the current elevation of the terraces, and their ages, it is then possible to determine a vertical uplift rate linked to the quaternary tectonic activity of the active faults (Woodroffe & Webster, 2014). In the case of significant tectonic uplift, the terraces are found tiered at several meters above the current sea level (e.g., in New Guinea (Chappell, 1974; Ota et al., 1993; Yokoyama et al., 2001), Gulf of Corinth (Armijo et al., 1996; de Gelder et al., 2019), Gulf of Aqaba (Bosworth et al., 2017; Manaa et al., 2016;

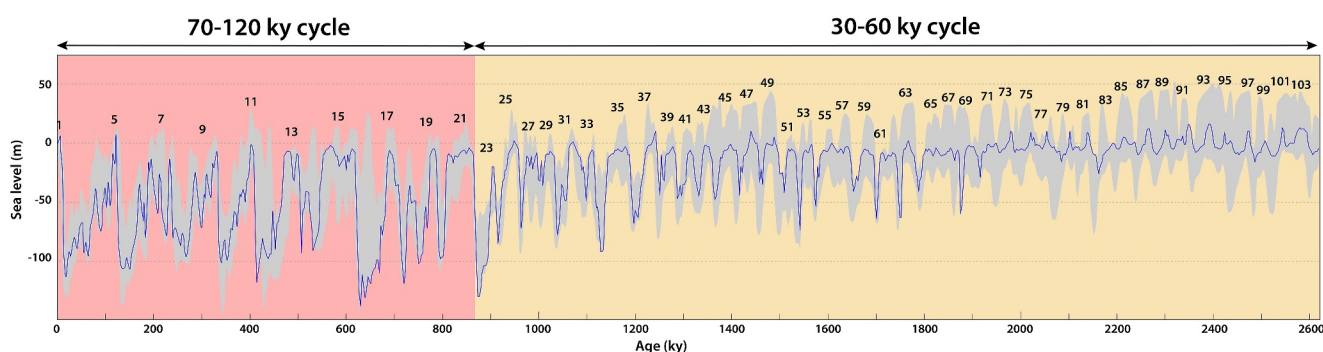


Figure 4. Composite curve of the sea level variations through the last 2.5 Myr showing the variations of the Marine Isotopic Stage across the Pleistocene. Lengthening and strengthening of the climatic cycle generate a modification of the record. Sea level data from 0 to 400 Kyr are from Siddall et al. (2003), data for >400 Kyr are from Bates et al. (2014). The gray envelopes correspond to all the other curves from the compilation of de Gelder et al. (2020) (see Figure S1 in Supporting Information S1).

Yehudai et al., 2017)). Conversely, with little or absence of tectonic activity, levels of terraces are found at the same elevation (e.g., in the Red Sea (Bantan et al., 2015; Khanna et al., 2021; Manaa et al., 2016; Plaziat et al., 1998, 2008)).

1.3. The Uplifted Terraces of the Gulf of Aqaba and Tiran Island

Along the Gulf of Aqaba and on Tiran Island, the well-preserved terraces provide a unique opportunity to study the vertical deformation of the coast of the gulf and of the island, and thus, the tectonic uplift along this strike-slip plate boundary.

To do so, we first proceed in the lateral correlation between the different sites located along the Gulf of Aqaba and the terraces preserved on Tiran Island (Figure 5), using high-resolution Digital Surface Model (DSM) all over the area. The U-Th ages on the different terraces (This study, Bar et al., 2018; Barnea et al., 2015; Bosworth et al., 2017; Manaa, 2016; Moustafa et al., 2000; Scholz et al., 2004; Shaked et al., 2011; Weil, 2008; Yehudai et al., 2017) confirm our lateral correlation between the sites along the gulf and we assume that the same sequence is reproduced on Tiran island at least for the lower levels. Second, from these observations, we propose an age model calibrated on the longer and higher sequence of the terraces of Tiran island and anchored with the absolute U-Th ages obtained from the terraces of the Gulf of Aqaba. Third, we apply this age model on the seven different sites spread over the entire eastern coast of the Gulf of Aqaba and derive the uplift rates on each site. The eustatic sea level variations are constrained using calibrated curves (Bates et al., 2014; Siddall et al., 2006), and the uncertainty on the sea level variations is established using the compilation from de Gelder et al. (2020) (Figure 4 and Figure S1 in Supporting Information S1). Last, we discuss this uplift rate in the regional framework and propose a mid/long-term vertical deformation scheme for the southern tip of the Dead Sea strike-slip fault system.

2. Methods

2.1. Digital Surface Model Derived From Pleiades Satellite Images

To map the height of the marine terraces, we built a DSM at 0.5-m ground resolution from high-resolution Pleiades satellite tri-stereo imagery using MicMac open-source software (see Text S2 in Supporting Information S1). The images were acquired in 2017 and 2018 (ref: ICR_FC_180915, ICR_FC_180916, ICR_FC_219129) over a total of 1,262 square kilometers along the eastern margin of the Gulf of Aqaba and on Tiran Island. The satellite optical images are greyscale panchromatic images.

In March 2017, we also acquired Differential Global Positioning System (DGPS) data on terrace levels to have absolute reference points along the gulf and to have a precise measurement of the tide. The DGPS data were processed using RTKLIB software. The absolute DSM calibration was then achieved by using the DGPS data and the sea level as a reference. We converted the DGPS data set into absolute points to allow a good positioning of the DSM vertically and horizontally as the absolute positioning errors of the DGPS are smaller than the resolution of the DSM (see Text S3 in Supporting Information S1). The maximal error on the horizontal position in our case is smaller than the maximal resolution of the DSM, that is, smaller than 50 cm. For the vertical positioning, the

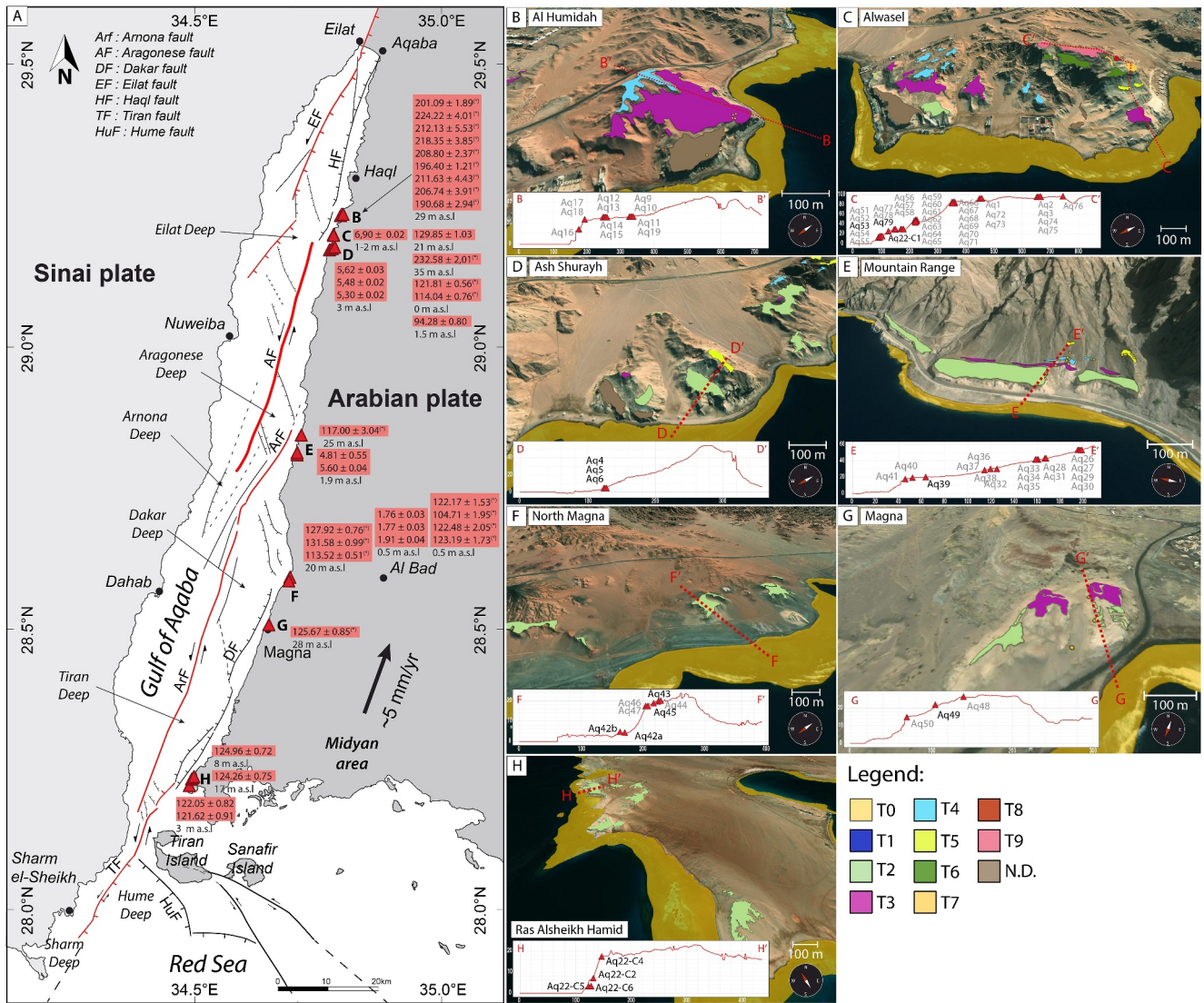


Figure 5. (a) Coral terrace sample locations (red triangles) with $^{230}\text{Th}/^{238}\text{U}$ ages of the eastern margin of the Gulf of Aqaba, see text for details. (b–h) 3D view of the sampling sites with the samples projected on a cross-section representative of the site. N.D., not defined. Samples in black are samples that were used for tectonic reconstruction, whereas samples in gray present signs of recrystallization and were not used further in the study.

DGPS data revealed a slight local distortion of the tiles and led to an uncertainty of the order of 1–3 m in height. For the DSM tiles with no DGPS, we used the overlapping neighboring tiles to correct the distortion and compute a fully referenced DSM.

For Tiran Island, the resulting elevation of the DSM is calibrated with the coastline obtained from the orthoimage. The vertical uncertainty of the MSL used as a reference is determined with the tide measurement realized by DGPS along the Gulf of Aqaba (see Text S3 in Supporting Information S1). The vertical resolution of the DSM was assessed by computing the average elevation of a 27,000 m² flat patch in the northern part of the island. Analyzing the standard deviation of the elevation, we derived an average vertical uncertainty of 0.87 m for our data on Tiran Island.

These DSM were later used to compute hillshades, slope maps, and contour maps using the GDAL open-source software. The shaded topography was calculated with an azimuth of N315°E or N135°E depending on the observed structure and with a low-angle altitude of the light source of 25°. We combined the results from the orthoimages and the maps derived from the DSMs, to map in detail the numerous marine terraces (see Figure S4 in Supporting Information S1). The presence of coral terraces is first identified based on their particularly whitish

color on the orthoimages and on their tabular shape. Then, the limits of the terraces are determined using the slope map and several topographic profiles in order to identify relatively flat areas delimited by abrupt topographic steps (see Figure S4 in Supporting Information S1). Finally the mapping has been refined locally during the sampling campaign, in particular to verify if in some places we observed both the FR and the RF of a single level.

Then, the average elevation of the terraces at each site has been extracted from the elevation of the DSMs. In Tiran island for each outcrop of coral terraces we extracted the elevation every 0.5 m to compute the average and median elevations and look at the dispersion of the elevation (see Figure S4 in Supporting Information S1).

2.2. Estimation of the Age of the Coral Terraces of the Gulf of Aqaba

The uplifted coral terraces of the Gulf of Aqaba were sampled in March 2017 and in March 2022. A total of 85 samples distributed along the eastern side of the Gulf of Aqaba have been collected at seven different sites, representing nine distinct terrace levels, from T1 near the current sea level to T9 at almost 100 m above the MSL (amsl). The samples along the gulf have been collected in the RF, while samples at the southern tip of the gulf have been collected, on purpose, either in the RF or in the FR areas. Before dating, each coral sample went through X-Ray Diffraction (XRD) at *GEOsciences Paris Sud* (GEOPS, France) to determine the different mineralogic fractions composing the skeleton of the coral sample (see Text S5 in Supporting Information S1).

2.2.1. Dating of Samples by $^{230}\text{Th}/^{234}\text{U}$ Method

$^{230}\text{Th}/^{234}\text{U}$ dating was performed at the *Laboratoire des Sciences du Climat* (LSCE, France). The amount of crushed material used for the analysis ranged between 10 and 200 mg. For selected samples, several sub-samples were taken to reach pristine zones and/or to be able to perform age modeling. After adding a triple ^{229}Th – ^{233}U – ^{236}U spike in a Teflon beaker, samples were dissolved with diluted HCl. The U-Th separation and purification were performed after coprecipitation with $\text{Fe}(\text{OH})_3$, on 0.6 ml columns filled with U-TEVA and pre-filter resins, in nitric media. The U and Th isotopic compositions were analyzed on a Multi-Collector Inductively Coupled Plasma source Mass Spectrometer (MC-ICPMS) Thermo Scientific™ Neptune^{Plus} fitted with a jet pump interface and a desolvating introduction system (aridus II). For mass fractionation correction, we used an exponential mass fractionation law (normalized to natural $^{238}\text{U}/^{235}\text{U}$ isotopic ratio) and standard/sample bracketing. More details on the analytical procedure (chemistry and MC-ICPMS analysis) can be found in Pons-Branchu et al. (2014). After corrections for peak tailing, hydrate interference, and chemical blanks, $^{230}\text{Th}/^{234}\text{U}$ ages were calculated from measured atomic ratios through iterative age estimation using the ^{230}Th , ^{234}U , and ^{238}U decay constants of Cheng et al. (2013) and Jaffey et al. (1971).

2.2.2. Selection Criteria

Eventually, we had to select a subset of meaningful ages among all the samples dated. This selection is based on a classical set of criteria that were adapted to the case of the Gulf of Aqaba:

- Since coral incorporates marine uranium, their isotopic signature should be compatible with the marine isotopic signature. This signature, documented by coral studies (Bard et al., 1990; Robinson et al., 2004; Scholz et al., 2004) is relatively constant for the last 500,000 years. Thus, a difference between initial uranium isotopic ratios calculated for the studied corals and the marine isotopic signature could be a sign of U uptake after coral skeleton formation, or a biased age (due to U or Th uptake/departure) (Bard et al., 1990; Hamelin et al., 1991). Therefore, we define that the calculated $^{234}\text{U}_{(0)}$ should lie within the strict range of $146.8 \pm 15\%$ (Chutcharavan et al., 2018; Tissot et al., 2018).
- XRD analysis is used to identify samples affected by diagenesis (aragonite to calcite transformation). However, in the case of pure aragonite, or with a small amount of calcite, the XRD is used together with the thin sections observation in order to detect possible secondary aragonite (see Figure S6 in Supporting Information S1). Combining the results of the thin sections and the diffractogram obtained by XRD, we recognized and discarded the samples presenting diagenesis alterations (Bar-Matthews et al., 1993; Lazar et al., 2004).
- In addition, the coral terraces have been formed mainly during periods with stable sea level (Lisiecki & Raymo, 2005) (Figure 4). Hence, the glacial terraces are formed during the low-stand periods, when the sea level is close to one hundred meters below the MSL, while the interglacial terraces are formed during the high-stand periods. In the Gulf of Aqaba, the tectonic activity of the DSF results in an uplift of the coast, and

subsequently an uplift of the coral terraces. We thus expect the terraces to get an age corresponding to the high-stand periods.

Eventually, U-series ages obtained from the coral samples that fulfill all these criteria were considered reliable and have been used further to determine the tectonic uplift of the Gulf of Aqaba. To retrieve additional ages, we calculated open-system ages following Thompson et al. (2003) model for samples presenting a $\delta^{234}\text{U}_{(0)}$ out of the determined ranges, but with the other criteria being validated.

2.3. Uplift Rate Determination

To constrain the tectonic uplift in the area, we need to determine the age of the terraces. Classically, when using marine terraces, the sea level is used as a reference, and the uplift rate is determined by $V_{\text{uplift}} = Z/T$, with Z the elevation of the terrace, corrected from the eustatic variations, and T the age of the terrace. To improve the age determination as the terraces get older, one could determine the uplift rate with $V_{\text{uplift}} = \Delta Z/\Delta T$, where ΔZ is the differential elevation between two terraces corrected from the eustatic variation and ΔT the time gap between two interglacial Marine Isotopic Stages (see Figure 3). This method will in addition limit the errors in the rate determination due to local variation of the terrace surfaces.

Because of the geochemical constraints (i.e., 500 Kyr limitation with the U series) and the impossibility to collect samples on Tiran Island, due to access restrictions, the age (T) of most of the terraces we can recognize on our DSM cannot be determined directly. On the other hand, thanks to our calibrated Pleiades DSM, the elevation (Z) of the entire eastern coast of the Gulf of Aqaba and Tiran Island is well-constrained. Morphologically, the terraces are visible everywhere and they present similar shapes and elevations along the gulf and on Tiran Island, allowing a good lateral correlation. Thus, we built an age model based on the eustatic curve, terrace elevation, and few anchor terraces along the gulf with absolute ages (T_1 , T_2 , and T_3), to estimate the ages of the upper terraces.

During most MIS periods, the development of marine terraces is modulated by small eustatic fluctuations called sub-stages. For the estimation of the time gap between the two terraces, we will consider that the preserved and uplifted terraces on Tiran Island are formed when the sea level is at its highest level during each MIS period considered. For the stages where the amplitudes of the sub-stages are similar (e.g., MIS 7, Figure 4), we will test the different possible ages and we will favor the one giving an uplift rate consistent with the upper and lower terraces.

Note that because the uplift rate is a local measurement, the values determined by the model might differ depending on the distance to the fault, the local structures (i.e., faults or gravitational disturbance, which can locally trigger higher or lower elevation values), or due to the different conditions of preservation of the terraces. We calibrated the model on the southwestern part of Tiran Island, where the record of the tectonic markers is the longest and the most regular, away from visible perturbations. If we move eastward or westward, we expect that the uplift rate might change, as the record of the marine terraces on the southern side of the island is scarce and the record on the western side of the island seems affected by the off-shore fault located in the Strait of Tiran.

3. Results

3.1. The Terraces of the Gulf of Aqaba

3.1.1. Map of the Aqaba Terraces

Terraces are visible along the Gulf of Aqaba. They are platforms mainly formed by the bio-construction of coral colonies. In some places, such as south of the city of Haql, a few levels correspond to erosional surfaces or wave-cut surfaces, without or with only a small cover of coral colonies. In both cases they display the typical morphology of a marine surface, namely a flat surface gently sloping seaward and limited at both ends by steep slopes.

In total, 9 fossil levels and 1 living level have been identified from the actual sea level (T_0) to almost 100 m amsl (T_9). The uplifted terraces have been sampled on seven different sites, namely: Al Humidah, Alwasel, Ash Shurayh, Mountain Range, North Magna, Magna, and Ras Alsheikh Hamid (Figure 5).

In the following, each terrace level is described in detail:

T0—The first level (*T0*), corresponds to the living platform and is present all along the gulf. The terrace width extends from 10 to 500 m. The maximal elevation of this level is defined by the amplitude of the low tide and is localized at 0.5 m below the current MSL.

T1—The second level (*T1*) is the first emerged level. Although this terrace could be found in many places along the coast, it is not showing the same continuity as *T0*. Its elevation ranges between 1 m and 3 m amsl (this study, Yehudai et al., 2017).

T2—The third level (*T2*) is the most visible and preserved level along the entire gulf. It has been found at each sampling site. The elevation of this platform is ranging from 3 to 26 m amsl (this study, Bosworth et al., 2017; Yehudai et al., 2017).

T3—The fourth level (*T3*) is also a well-preserved level along the gulf. Sometimes this level is the most preserved terrace (e.g., in Al Humidah), while at other sites this level is partly or totally buried under slope deposits and only a small cliff marks the location of the terraces (e.g., in Alwasel or Mountain Range). The elevation of this level ranges from 22 to 32 m amsl (this study, Yehudai et al., 2017).

T4 & T5—The fifth level (*T4*) and the sixth level (*T5*) are only visible on the Al Humidah, Alwasel, Ash Shurayh, and Mountain Range sites. They are fairly undeveloped and scarce, making the lateral correlation difficult. Their elevation ranges respectively between 30 and 45 m amsl and between 50 and 56 m amsl.

T6, T7, T8 & T9—The terraces from the seventh level (*T6*) to the tenth level (*T9*) are only found at the Alwasel site. They are mostly covered by slope deposits. *T6* is a prominent level, clearly visible. Relics preserved from erosion of *T7* and *T8* have been observed on the field at the edge of the site and are distinguishable thanks to the slope break along their edge. *T9* is the flat preserved level at the top of the site. Their elevation ranges respectively between 75 and 79 m amsl, between 82 and 86 m amsl, between 87 and 90 m amsl, and between 93 and 97 m amsl.

3.1.2. $^{230}\text{Th}/^{234}\text{U}$ Chronology of Corals

According to the criteria presented in Section 3.2.2, we have measured $^{230}\text{Th}/^{234}\text{U}$ ages on 24 samples (Tables 1 and 2). Among the 36 $^{230}\text{Th}/^{234}\text{U}$ analyses, including 12 duplicates, some inconsistency can be expected, for example, due to remobilization of a sample from the overlying terraces onto a lower one, or the presence of secondary aragonite undetected by the XRD, and revealed by thin sections analyses of our corals (see Figure S6 in Supporting Information S1).

Based on other studies in the area (e.g., Bar et al., 2018; Barnea et al., 2015; Bosworth et al., 2017; Manaa, 2016; Moustafa et al., 2000; Scholz et al., 2004; Shaked et al., 2011; Weil, 2008; Yehudai et al., 2017), the consensus is that the terraces ranging on an elevation of ~ 20 m amsl correspond to the MIS 5 terraces, while the terraces ranging at an elevation of ~ 2 m amsl correspond to the MIS 1 terrace. Hence, we can sort out our ages to select only the ones that are consistent with the regional framework.

In Alwasel, the samples Aq 51, Aq 52, and Aq 55 are located at the outlet of a small wadi (see Figure 5c) at an elevation of ~ 1 m amsl and they yield a $^{230}\text{Th}/^{234}\text{U}$ age (90–120 Kyr) consistent with the MIS 5 terraces, while sample Aq 53 yields a $^{230}\text{Th}/^{234}\text{U}$ age of ~ 6.90 Kyr consistent with the MIS 1 terraces. On the sites of Ash Shurayh and Mountain Range, samples Aq 4, Aq 5, Aq 6, Aq 24, and Aq 25 yield an average $^{230}\text{Th}/^{234}\text{U}$ age of ~ 5.4 Kyr for an elevation between 2 and 3 m. In parallel, in North Magna, sample Aq 42a, standing at an elevation of ~ 1 m amsl, presents a $^{230}\text{Th}/^{234}\text{U}$ age of ~ 120 Kyr, while sample Aq 42b, at the same location, yields a $^{230}\text{Th}/^{234}\text{U}$ age of ~ 2 Kyr. Following the consensus on the ages of the terraces in the area, we assume that the samples Aq 51, Aq 52, Aq 55, and Aq 42a present ages inconsistent with the regional temporal framework and should be discarded.

In addition to this problem of remobilization, in some cases, the presence of recrystallization leads to a possible under/over-estimation of the real age of the terrace. Indeed, thanks to the high porosity of the coral, the local dissolution and precipitation of the calcium carbonate lead to the remobilization of the uranium and, consequently, to a bias in the age, although the samples seem to be chemically fine according to our first set of criteria. As already discussed by several authors, the departure of ^{238}U (parent isotope in the U-series) can be interpreted to be due to the leaching of the terraces with freshwater (Bar et al., 2018; Lazar & Stein, 2011; Yehudai et al., 2017). It would lead to a decrease in the apparent age. Conversely, the incorporation of ^{238}U leads to an increase in the apparent age.

Table 1

Coral Samples From the Interglacial Marine Terraces of the Eastern Side of the Gulf of Aqaba

Lab N°	Sample name	Site name	Reef zone	Latitude	Longitude	Ar %	Elev. (m)	Terrace
7412	Aq 4	Ash Shurayh	RF	29.160256	34.892588	99	3	T1
7413	Aq 5	Ash Shurayh	RF	29.160256	34.892588	99	3	T1
7414	Aq 6	Ash Shurayh	RF	29.160256	34.892588	99	3	T1
7456	Aq 13a (1)	Al Humidah	RF	29.219663	34.911136	95	29	T3
8728	<i>Aq 13a (2)</i>							
8729	<i>Aq 13a (3)</i>							
8730	<i>Aq 13a (4)</i>							
7457	Aq 13b (1)	Al Humidah	RF	29.219663	34.911136	98	29	T3
7783	<i>Aq 13b (2)</i>							
8731	<i>Aq 13b (3)</i>							
8732	<i>Aq 13b (4)</i>							
7502	Aq 15 (1)	Al Humidah	RF	29.219754	34.911071	99	29	T3
7458	Aq 24	Mountain Range	RF	28.754732	34.811218	99	1.9	T1
7415	Aq 25	Mountain Range	RF	28.754566	34.812031	99	1.9	T1
7503	Aq 39	Mountain Range	RF	28.779977	34.819854	85	25	T2
7504	Aq 42a (1)	North magna	RF	28.505278	34.795833	99	0.5	T1
8682	<i>Aq 42a (2)</i>							
8726	<i>Aq 42a (3)</i>							
8727	<i>Aq 42a (4)</i>							
7505	Aq 42b (1)	North magna	RF	28.505278	34.795833	99	0.5	T1
7784	<i>Aq 42b (2)</i>							
7788	<i>Aq 42b (3)</i>							
7416	Aq 43 (1)	North magna	RF	28.50684	34.795817	80	20	T2
7531	<i>Aq 43 (2)</i>							
7418	Aq 45	North magna	RF	28.506984	34.795759	99	20	T2
7507	Aq 49	Magna	RF	28.420422	34.752969	80	28	T2
7421	Aq 51	Alwasel	RF	29.185221	34.896122	99	0	T1
7422	Aq 52	Alwasel	RF	29.18489	34.895919	99	0	T1
7423	Aq 53	Alwasel	RF	29.183444	34.895387	90	1.5	T1
7425	Aq 55	Alwasel	RF	29.185082	34.89618	98	1.5	T1
7472	Aq 79	Alwasel	RF	29.1829	34.89636	85	35	T3
10130	Aq22-C1	Alwasel	RF	29.189888	34.900806	N.D.	21	T2
10131	Aq22-C2	Ras Alsheikh Hamid	FR	28.096241	34.572124	N.D.	8	T2
10132	Aq22-C4	Ras Alsheikh Hamid	RF	28.107457	34.574529	N.D.	17	T2
10134	Aq22-C5	Ras Alsheikh Hamid	FR	28.112067	34.578126	N.D.	3	T2
10135	Aq22-C6	Ras Alsheikh Hamid	FR	28.112067	34.578126	N.D.	3	T2

Note. Duplicates from different coral pieces are in italic. Elevations are local measurements. RF, Reef Flat; FR, Fore Reef.

In our case, the ages for the samples from the terrace T1 (Aq 4, Aq 5, Aq 6, Aq 24, Aq 25, 42b, and Aq 53) range between 1.76 and 6.9 Kyr for an elevation ranging between 0.5 and 3 m. Even if the age of sample Aq 42b is a bit young (~1.7 Kyr), the ages from the terrace T1 are consistent with the development of a coral terrace during the Holocene, after the last glacial maximum, when the sea level is close to the current MSL (Shaked et al., 2011; Woodroffe et al., 2012).

Table 2
Result of the $^{230}\text{Th}/^{234}\text{U}$ Analyses: U and Th Content and Isotopic Ratios

Sample name	Terrace	^{238}U ppm		^{232}Th ppb		$\delta^{234}\text{U}_M$ (‰)				$^{230}\text{Th}/^{238}\text{U}$		$^{230}\text{Th}/^{232}\text{Th}$		$\delta^{234}\text{U}_T$ (‰)		Age (Kyr)	Final age (Kyr)
Aq 4	T1	2.752	0.022	0.069	0.001	139.2	1.0	0.0548	0.0001	6,725.3	15.0	141.3	1.0	5.30	0.02	5.30	0.02
Aq 5	T1	2.329	0.019	0.036	0.000	142.8	0.9	0.0567	0.0001	11,265.8	22.5	145.1	1.0	5.48	0.02	5.48	0.02
Aq 6	T1	2.357	0.019	0.283	0.002	138.1	1.2	0.0581	0.0001	1,477.0	2.9	140.3	1.2	5.62	0.03	5.62	0.03
Aq 13a (1)	T3	3.160	0.025	0.131	0.001	113.2	1.1	1.0143	0.0021	74,134.2	116.8	221.8	2.7	237.91	2.61	201.09*	1.89
Aq 13a (2)		<i>3.361</i>	<i>0.027</i>	<i>8.509</i>	<i>0.070</i>	<i>89.0</i>	<i>1.9</i>	<i>0.9882</i>	<i>0.0040</i>	<i>1,223.3</i>	<i>4.9</i>	<i>174.8</i>	<i>4.6</i>	<i>238.91</i>	<i>5.15</i>	<i>224.22*</i>	<i>4.01</i>
Aq 13a (3)		<i>3.086</i>	<i>0.025</i>	<i>15.290</i>	<i>0.140</i>	<i>98.6</i>	<i>3.2</i>	<i>0.9939</i>	<i>0.0045</i>	<i>628.7</i>	<i>2.8</i>	<i>191.5</i>	<i>7.1</i>	<i>234.78</i>	<i>6.41</i>	<i>212.13*</i>	<i>5.53</i>
Aq 13a (4)		<i>3.193</i>	<i>0.026</i>	<i>3.046</i>	<i>0.027</i>	<i>92.6</i>	<i>1.9</i>	<i>0.9880</i>	<i>0.0040</i>	<i>3,283.7</i>	<i>13.0</i>	<i>180.1</i>	<i>4.5</i>	<i>235.60</i>	<i>4.94</i>	<i>218.35*</i>	<i>3.85</i>
Aq 13b (1)	T3	4.974	0.040	0.225	0.002	82.9	1.2	0.9428	0.0029	63,238.0	152.5	150.2	2.6	210.48	2.79	208.80*	2.37
Aq 13b (2)		<i>4.582</i>	<i>0.037</i>	<i>0.129</i>	<i>0.001</i>	<i>83.4</i>	<i>0.9</i>	<i>0.9185</i>	<i>0.0006</i>	<i>104,160.3</i>	<i>72.5</i>	<i>144.8</i>	<i>1.5</i>	<i>195.36</i>	<i>0.87</i>	<i>196.40*</i>	<i>1.21</i>
Aq 13b (3)		<i>4.145</i>	<i>0.034</i>	<i>34.136</i>	<i>0.300</i>	<i>76.3</i>	<i>2.5</i>	<i>0.9290</i>	<i>0.0043</i>	<i>357.6</i>	<i>1.6</i>	<i>136.5</i>	<i>4.8</i>	<i>205.82</i>	<i>4.57</i>	<i>211.63*</i>	<i>4.43</i>
Aq 13b (4)		<i>4.461</i>	<i>0.036</i>	<i>19.816</i>	<i>0.174</i>	<i>77.9</i>	<i>2.2</i>	<i>0.9238</i>	<i>0.0043</i>	<i>659.3</i>	<i>3.0</i>	<i>137.7</i>	<i>4.2</i>	<i>201.76</i>	<i>4.13</i>	<i>206.74*</i>	<i>3.91</i>
Aq 15 (1)	T3	4.600	0.038	0.145	0.001	86.7	1.9	0.9154	0.0038	87,497.4	364.4	149.1	3.5	191.73	3.13	190.68*	2.94
Aq 24	T1	2.813	0.023	10.653	0.086	151.2	1.4	0.0621	0.0008	49.9	0.6	153.3	1.5	4.81	0.55	4.81	0.55
Aq 25	T1	2.262	0.018	0.218	0.002	145.9	1.1	0.0583	0.0002	1,983.3	7.4	148.3	1.1	5.60	0.04	5.60	0.04
Aq 39	T2	6.077	0.051	2.245	0.020	119.3	3.5	0.7849	0.0029	7214.8	26.5	171.1	5.0	127.48	1.74	117.00*	3.04
Aq 42a (1)	T1	2.282	0.018	0.429	0.004	104.5	1.8	0.7562	0.0025	12,052.0	39.9	147.8	2.6	122.46	1.15	122.17*	1.53
Aq 42a (2)		<i>2.207</i>	<i>0.018</i>	<i>25.701</i>	<i>0.215</i>	<i>124.0</i>	<i>2.7</i>	<i>0.7418</i>	<i>0.0025</i>	<i>192.9</i>	<i>0.7</i>	<i>171.1</i>	<i>3.8</i>	<i>113.92</i>	<i>1.47</i>	<i>104.71*</i>	<i>1.95</i>
Aq 42a (3)		<i>2.328</i>	<i>0.019</i>	<i>20.453</i>	<i>0.174</i>	<i>99.5</i>	<i>2.4</i>	<i>0.7406</i>	<i>0.0024</i>	<i>256.1</i>	<i>0.8</i>	<i>139.2</i>	<i>3.4</i>	<i>118.79</i>	<i>1.43</i>	<i>122.48*</i>	<i>2.05</i>
Aq 42a (4)		<i>2.197</i>	<i>0.018</i>	<i>10.284</i>	<i>0.086</i>	<i>101.5</i>	<i>1.9</i>	<i>0.7504</i>	<i>0.0035</i>	<i>487.2</i>	<i>2.3</i>	<i>143.1</i>	<i>2.7</i>	<i>121.36</i>	<i>1.54</i>	<i>123.19*</i>	<i>1.73</i>
Aq 42b (1)	T1	3.218	0.026	0.328	0.003	156.5	2.6	0.0195	0.0001	581.1	3.7	157.3	2.6	1.76	0.03	1.76	0.03
Aq 42b (2)		<i>3.032</i>	<i>0.024</i>	<i>0.335</i>	<i>0.003</i>	<i>156.2</i>	<i>0.6</i>	<i>0.0188</i>	<i>0.0001</i>	<i>542.6</i>	<i>4.3</i>	<i>156.9</i>	<i>0.6</i>	<i>1.77</i>	<i>0.03</i>	<i>1.77</i>	<i>0.03</i>
Aq 42b (3)		<i>3.054</i>	<i>0.024</i>	<i>0.351</i>	<i>0.003</i>	<i>158.1</i>	<i>0.8</i>	<i>0.0204</i>	<i>0.0003</i>	<i>598.5</i>	<i>9.5</i>	<i>159.0</i>	<i>0.8</i>	<i>1.91</i>	<i>0.04</i>	<i>1.91</i>	<i>0.04</i>
Aq 43 (1)	T2	2.568	0.021	1.021	0.008	111.5	0.8	0.8011	0.0017	6,631.0	13.7	163.1	1.2	134.47	0.78	127.92*	0.76
Aq 43 (2)		<i>2.347</i>	<i>0.019</i>	<i>1.144</i>	<i>0.009</i>	<i>114.0</i>	<i>1.1</i>	<i>0.8228</i>	<i>0.0011</i>	<i>5,064.5</i>	<i>6.7</i>	<i>169.8</i>	<i>1.7</i>	<i>140.93</i>	<i>0.75</i>	<i>131.58*</i>	<i>0.99</i>
Aq 45	T2	3.068	0.025	2.169	0.017	127.1	0.7	0.7917	0.0007	3,425.2	2.9	182.3	1.0	127.51	0.44	113.52*	0.51
Aq 49	T2	2.456	0.020	0.108	0.001	116.0	0.9	0.8064	0.0018	54,875.7	121.8	169.9	1.4	135.08	0.81	125.67*	0.85
Aq 51	T1	2.224	0.018	0.086	0.001	101.8	0.5	0.7455	0.0017	63,149.4	148.1	142.8	0.7	120.02	0.61	121.81*	0.56
Aq 52	T1	2.220	0.018	0.120	0.001	110.2	0.8	0.7397	0.0020	44,997.6	122.9	153.2	1.2	116.57	0.74	114.04*	0.76
Aq 53	T1	2.886	0.023	0.189	0.002	138.5	0.7	0.0707	0.0001	3,297.0	5.3	141.2	0.7	6.90	0.02	6.90	0.02
Aq 55	T1	2.861	0.023	4.287	0.037	113.6	0.7	0.6543	0.0023	1,442.0	5.0	148.3	1.0	94.28	0.80	94.28	0.80
Aq 79	T3	2.953	0.024	0.137	0.001	57.2	1.1	0.9107	0.0007	59,470.5	48.2	102.8	2.1	207.31	1.28	232.58*	2.01
Aq22-C1	T2	2.120	0.017	0.376	0.004	106.9	1.4	0.7822	0.0021	13,743.5	36.9	154.2	2.0	129.85	1.03	129.85	1.03
Aq22-C2	T2	2.347	0.019	0.098	0.001	102.7	0.8	0.7628	0.0018	56,768.4	128.9	146.2	1.2	124.96	0.72	124.96	0.72
Aq22-C4	T2	2.980	0.024	1.171	0.009	108.0	1.0	0.7649	0.0016	6,057.1	12.4	153.4	1.5	124.26	0.76	124.26	0.75
Aq22-C5	T2	2.457	0.020	0.145	0.001	107.1	1.2	0.7563	0.0018	40,154.2	95.9	151.2	1.8	122.05	0.82	122.05	0.82
Aq22-C6	T2	1.990	0.016	0.072	0.001	105.9	1.6	0.7539	0.0019	65,192.8	161.0	149.4	2.2	121.62	0.91	121.62	0.91

Note. Duplicates from different coral pieces are in italic. Ages were corrected for detrital fraction, with a $(^{230}\text{Th}/^{232}\text{Th})_0 = 7 \pm 3.5$. Final ages with * are calculated open-system ages following Thompson et al.'s (2003) model. The final ages in blue are the ones that fulfill all the criteria presented above, bold ages are the selected ages to build the age model (see main text for further details).

The ages of samples from the terrace T2 (Aq 39, Aq 43, Aq 45, Aq 49, Aq22-C1, Aq22-C2, Aq22-C4, Aq22-C5, and Aq22-C6) range between 113 and 131 Kyr for an elevation ranging between 20 and 28 m. The ages of the terrace T2 are consistent with the development of a coral terrace during the MIS 5e substage (117–131 Kyr). During the MIS 5e the sea level was oscillating between +5 m from the current MSL at 125 Kyr and –5 m from the current MSL at 119 Kyr in the Red Sea-Gulf of Aqaba area (Rohling et al., 2009; Siddall et al., 2003). The age

diversity found on some samples of this level also suggests that some of the samples present signs of early-stage recrystallization.

In the southern part of the gulf, at Ras Alsheikh Hamid, the terrace T2 is different in terms of geometry and preservation compared to the other sites along the gulf. We observed large levels slightly dipping toward the gulf. The five samples from the area located at elevations between 3 and 21 m give ages between 121 and 129 Kyr confirming that all the terrace surfaces formed during the MIS 5e and correspond to T2. We think that in Ras Alsheikh Hamid both the RF and the FR are preserved and were sampled, explaining the wide range of elevation for this level.

The samples from the terrace T3 (Aq 13a, Aq 13b, Aq 15, and Aq 79) yield ages between 191 and 232 Kyr for an elevation ranging between 29 and 35 m. The ages of the T3 samples are consistent with the development of the terrace T3 during MIS 7. Samples Aq 13a, Aq 13b, and Aq 15 point to the formation of the terrace during the MIS 7a substage (190–203 Kyr), while the age of sample Aq 79 agrees with a terrace formed during the MIS 7e substage (233–243 Kyr). During the MIS 7a and 7e, the sea level was respectively -2 m and -5 m below the current sea level (Grant et al., 2007; Rohling et al., 2009; Siddall et al., 2003). Considering that the samples are also exposed to an early recrystallization stage event after the formation of the terrace, we assume that the age of the terrace T3 in the Gulf of Aqaba may correspond to the MIS 7e, even if most of the samples suggest that the terraces were established during the MIS 7a.

Eventually, a total of 16 samples out of the 24 (see Table 2) are useable for the determination of the tectonic uplift in the Gulf of Aqaba.

3.2. The Terraces on Tiran Island

The marine terraces preserved on Tiran Island are similar to the uplifted coral terraces from the Gulf of Aqaba. The terraces are visible along the south-western shore of Tiran Island where they mainly correspond to depositional platforms formed by bio-construction of coral colonies. Along the isthmus separating the northern part from the southern part of the island, the terraces rather correspond to erosional surfaces (or wave-cut surfaces). In most cases, they display the typical morphology of a marine terrace, that is a flat surface gently sloping seawards and limited at both ends by steep slopes. The succession of marine terraces imprints the landscape morphology like the succession of steps.

Following this definition, we mapped in detail the coral terraces visible all along Tiran Island. At least 19 levels of marine coral terraces are preserved along the southwestern side of the island, from 1 m to almost 500 m above the MSL. The terraces are narrow and do not exceed 100 m in width (Figure 6).

Hereafter, we describe the successive levels of terraces and we highlight the characteristics of each level.

3.2.1. General Description of the Tiran Terraces

T0—The first level (Level 0) corresponds to the living coral platform. It is found all around Tiran Island. On the northern side of the island, the terrace T0 reaches nearly 5,000 m in width between Tiran island and the continent at Ras Gasabah (Ras Qisbah) and Ras Alsheikh Hamid. Conversely, along the southern coast of the island, the platform is narrower, between 10 and 130 m in width.

T1—Level 1 is the first emerged level found along Tiran island. It is a fairly undeveloped level, locally marked by a coral terrace, or a marine notch. This level is visible near Foul Bay and the isthmus separating the northern part from the southern part of the island (Figure 6). It becomes more scattered in the southwest part of the island and is no longer visible along the southern coast. This level stands between 1 and 5 m amsl.

T2—Level 2 is the most visible and well-developed level along the western and southern coasts of the island. This level is continuous and it is used as a benchmark level during the lateral correlation along the island. Its elevation gradually changes from ~ 25 to ~ 15 m amsl from west to east, reflecting a tilt of the terrace toward the east. It is around 24 m above level 1. To the west, level 2 corresponds to a wave-cut terrace where it is directly carved in sandstone (probably Miocene) with only very limited or even no coral cap (see Figure S7 in Supporting Information S1). In the south, the coral terraces are established on top of sandstones (probably Miocene) and limestones (probably Pliocene) deposits (Figure 1c).

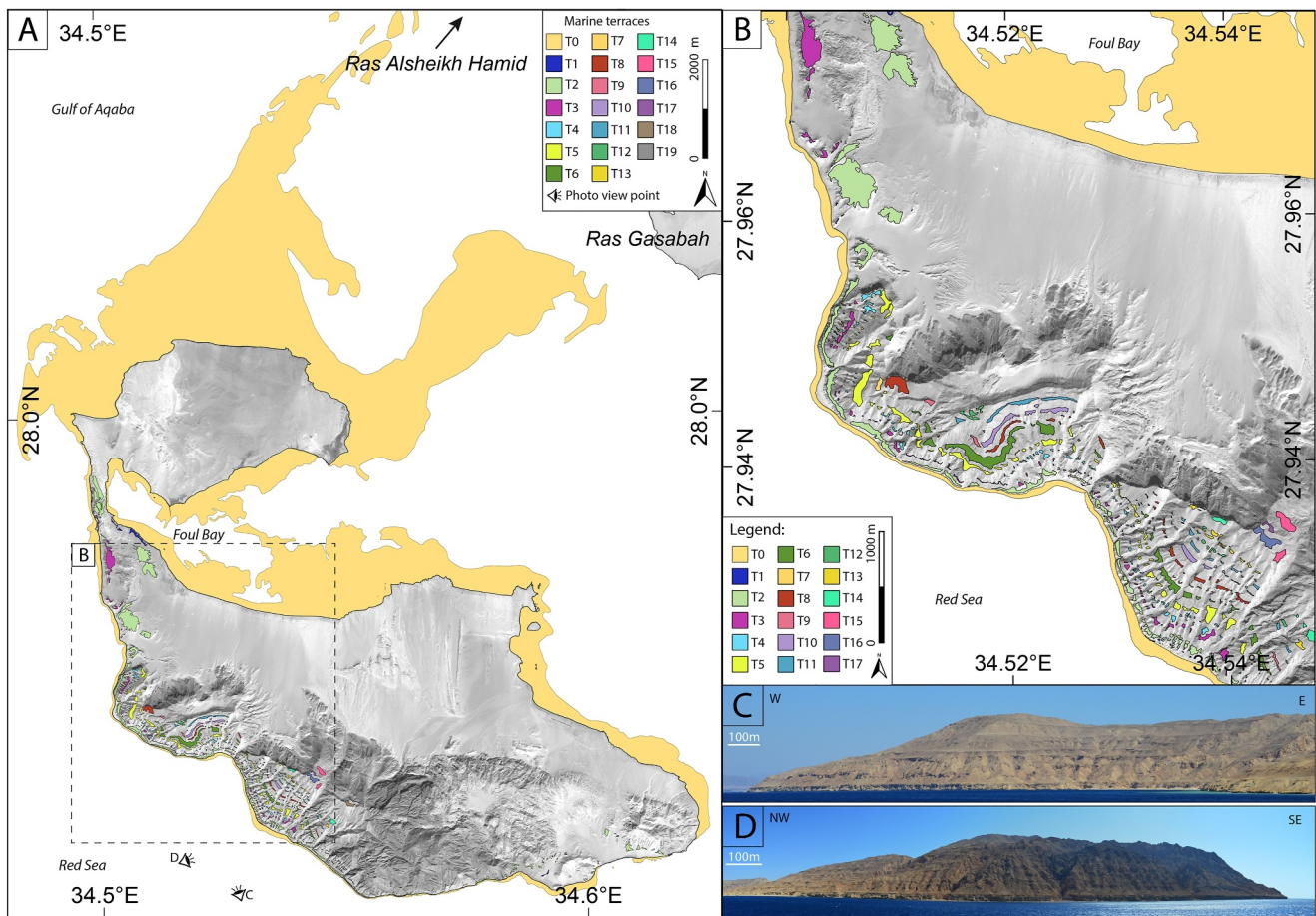


Figure 6. (a) Map of the uplifted coral terraces along the southwestern part of Tiran Island superimposed on a high-resolution Pleiades satellite image. (b) Zoom of the west of Tiran Island, see location in (a), with coral terraces ranging from 0 to almost 500 m above the mean sea level. (c, d) Lateral views of the Tiran Island terraces.

T3—Level 3 is located between 40 and 45 m amsl, and around ~20 m above Level 2. This level, less visible than the previous one, is present in the western and southwestern parts of the island. It extends from a few meters to several tens of meters in width.

T4—Level 4 is found only along the southwestern edge of Tiran Island, at an elevation ranging from 50 to 70 m amsl. It is located around 10 m above level 3. Level 4 ranges between 25 and 40 m in width. Its elevation is not constant, and it is higher in the west than in the east, which is consistent with a tilt of the terrace toward the east.

T5—Level 5 is located southwest of the island, at an average elevation of 80 m amsl on the southwest side and an average elevation of 110 m amsl on the west side. This level is a benchmark level along the island. This level is about 20 m above level 4. It is on average between 20 and 60 m in width, and locally up to 150 m. Its elevation from west to east gradually decreases showing a pronounced tilt of the terrace toward the east.

T6—Level 6 is located southwest of the island, at an average elevation of 97 m amsl on the southwest side and an average elevation of 130 m amsl on the west side. Like level 5, it is a benchmark level along the island. Level 6 is about 17–20 m above level 5. Level 6 is well-developed and easy to recognize in the landscape. It is on average between 20 and 80 m in width. This level shows a significant variation in its lateral elevation. This shift in the elevation shows a tilt of the terrace toward the east.

T7—Level 7 is difficult to identify. It is outcropping only along the southwestern edge of the island over a width of a few meters, between 110 and 120 m amsl. Level 7 is located about 10 m above level 6. The lack of lateral continuity of T7 hinders the possibility to quantify any tilting.

T8—Level 8 is found in the southwestern part of Tiran Island, at an elevation ranging between 140 and 160 m amsl and, on average, 30 m above Level 7. The terrace is well-preserved and developed on a swath of 25 m on average. To the west, the terrace covers an area of 20,000 m². The general trend of the terrace shows a decrease in the elevation values toward the east, indicating a tilt toward the east.

T9—Level 9 is not well preserved along Tiran Island, possibly mostly eroded or buried under slope deposits. It is only visible in three places along the southwestern part of the island with an elevation gradually passing from 188 to 150 m amsl while moving eastward.

T10—Level 10 is found only along the southwestern edge of Tiran Island, at an elevation of 192 m amsl. This level extends from 10 to 50 m in width. The topographic difference with Level 8 is around 47 m.

T11—Level 11 is found only along the southwestern edge of Tiran Island at an elevation varying between 225 and 240 m amsl, and on average 40 m above level 10. This level is approximately 20 m wide. It is not possible to determine whether the terrace presents a tilt to the east or not.

T12—Level 12 is observed at 240 m amsl in the southeastern part of the island. On the western side its elevation increases gradually and reaches locally 274 m amsl. This level is rather narrow, 20 m wide on average and only present along the southwest part of the island.

T13—Level 13 is located only on the southeastern part of the island, on average at 270 m amsl. This level is 20 m wide. It is located about 30 m above level 12. The limited lateral extension of the terrace does not allow us to determine if the terrace presents any tilting.

T14—Level 14, is found on the southwestern part of Tiran Island. It is a well-developed level, although not well preserved. It is located at an elevation varying between 297 and 310 m amsl. Approximately 5 m of slope deposits (colluvium) are found on the terrace. It is not possible to determine if the level is tilted. Level 14 is between 27 and 40 m above level 13.

T15—Level 15 is a well-developed level, although not very preserved. It is found in the southwest part of the island, at an average elevation of 325 m amsl. This level is between 60 and 90 m in width. The geographical extension of this level does not allow us to determine if it presents any tilt. This level is 15 m above Level 14.

T16—Level 16 is at an elevation between 350 and 355 m amsl. The level 16 is about 60–100 m in width. The difference in elevation from Level 15 is about 25 m. The average trend shows a decrease of elevation as we move southeastwards, indicating a tilt of the terrace.

T17—Level 17 is one of the highest levels of Tiran Island. It stands at an elevation of 367 m amsl and it is 20–50 m in width. Its small geographic extent does not make it possible to find any evidence of tilting. The difference in elevation with level 16 is about 17 m.

T18—Level 18 culminates at about 494 m amsl. It is one of the last markers of the tectonic uplift of the island. It is nearly 127 m apart from the underlying terrace (level 17). This level is between 30 and 60 m in width. As the geographic extent of this level is limited, it is not possible to determine whether it tilts eastward like the lower levels.

T19—Level 19 is the topmost level found on the island. It culminates between 514 and 517 m amsl. This terrace is located at the summit of the island over an area of 0.012 km². It presents the same morphology as level 18 and it is about 20 m above the latter.

The presence of the terraces only along the south and southwestern side of the island emphasizes that the fault responsible for the uplift of the whole sequence of terraces on Tiran Island is located south of the island. In addition to this, the terraces that have the largest lateral extent present an increase of their elevation toward the west, suggesting a tilt eastward. This tilt seems to increase when moving higher up the fly of terraces. Thus, the geometry of the terraces outlines that the deformation of Tiran Island likely results from the combination of the effects due to two different fault systems.

3.2.2. Age of the Tiran Terraces

Assuming that the terraces present along Tiran Island conform to the sequence present along the Gulf of Aqaba, the estimation of the age of the lower levels of Tiran Island is made from the dating realized along the Gulf of Aqaba.

Indeed, the first level (T1) is similar to the one found along the Gulf of Aqaba (Al-Rifaiy & Cherif, 1988; Bar et al., 2018; Lazar & Stein, 2011; Lazar et al., 2004; Moustafa et al., 2000; Scholz et al., 2004; Shaked et al., 2004) that is a Holocene terrace, dated at 5.9 Kyr (Figure 5).

Level 2 (T2), also found along the coast of the Gulf of Aqaba with the same characteristics, was dated to the MIS 5 (Figure 5). Even if during the MIS 5 the development of marine terraces is modulated by small eustatic fluctuations, which lead to three different sub-stages (5a, 5c, and 5e), along the Gulf of Aqaba and surroundings of the Strait of Tiran, several studies (Bar et al., 2018; Bosworth et al., 2017; Gvirtzman et al., 1992; Manaa et al., 2016; Taviani et al., 2019; Yehudai et al., 2017) estimated the age of the mean 20 m amsl marine terrace at 119–125 Kyr. Consequently, on Tiran Island, we assume that level 2 (T2) at 20 m amsl also corresponds to the main spike of the MIS 5e.

West of the Foul Bay, an intermediate level in-between level 1 and level 2, at an elevation ranging between 5 and 8 m is preserved. This level is also found in several places along the Gulf of Aqaba and displays ages consistent with the MIS 5e (see samples AQ22-C5 and AQ22-C6 in the Ras Alsheikh Hamid site).

Level 3 (T3) is also visible in some places along the Gulf of Aqaba (Figure 5), where it has been dated to the MIS 7. Several authors, based on $^{230}\text{Th}/^{234}\text{U}$ dating (this study; El-Asmar, 1997; Gvirtzman et al., 1992; Yehudai et al., 2017) estimated an age of ~200 Kyr, during the MIS 7a. However, the age of the sample Aq 79 (232 ± 2 Kyr) agrees with development during the MIS 7e substage, thus at this stage, we cannot rule out an older age associated with the MIS7e for the level 3 on Tiran Island.

Because no absolute dating has been proposed for the higher terraces in the surroundings of the Gulf of Aqaba and Strait of Tiran areas, we propose to use relative chronology to estimate the age of the upper terraces on Tiran Island.

The morphology of the uplifted terraces seems to be influenced by the Milankovitch climatic cycles (i.e., 120 Kyr cycles), and the general trend of the three first levels (T1, T2, and T3) correlates with the last three main interglacial peaks (MIS 1, MIS 5, and MIS 7). For level 4 (T4), level 5 (T5), level 6 (T6), level 7 (T7), and level 8 (T8), the differential elevation between each level remains constant. Following the beginning of the sequence and considering a cyclic development of the terraces during the interglacial periods, we assume that the terraces must respectively correlate with the MIS 9, MIS 11, MIS 13, MIS 15, and MIS 17.

From level 10 (T10), relative dating is no longer possible since the gap in elevation between the different levels becomes too large, thus the glacial-interglacial cycle does not correlate anymore with the terrace succession.

3.2.3. Age Model

The elevation differences between subsequent terraces, ranging from T0 to T8, correlates with the successive MIS observed over the past 700 Kyr. However, starting from T10, the vertical distance between these terraces becomes uncertain, making it impossible to establish a correlation with their respective MIS sequences. Nonetheless, Tiran Island presents additional terrace levels, which can be used to estimate the uplift rate of the area.

To do so, we consider different models assuming that the island terrace record is complete or not. The number of preserved terraces varies along the coast, and thus we built our models based on the morphology observed on the southeastern part of the island, where the terraces sequence is the most important.

The first model (Figure 7a) is built assuming a complete record of the eustatic cycle by the marine terraces of Tiran Island. Each terrace developed during a high-stand period is preserved along Tiran Island, which leads to record 19 MIS periods from the MIS 1 terraces (Level 1–5.7 Kyr) to the MIS 49 (Level 19–1.5 Myr). As the distance between terraces is changing, the result of this first age model involves a sudden change of the uplift rate between MIS 21 and MIS 23, from 0.81 ± 0.11 mm/year during the mid-Pleistocene, to 0.20 ± 0.02 mm/year since the upper-Pleistocene (see Figure S8 in Supporting Information S1).

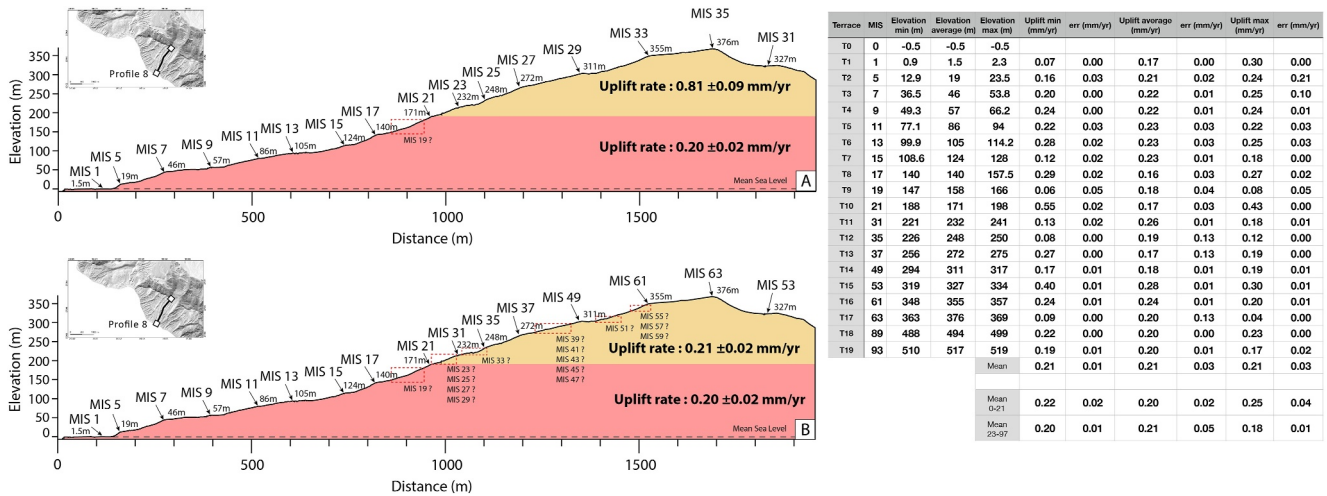


Figure 7. Age models of Tiran Island based on the analysis of the Pleistocene terraces recorded on the island. (a) Age model based on the assumption of a complete record (every high sea level period) of the coral terraces. Level 9 (red dashed square) is not visible along this profile. (b) Age model considering an incomplete record of the coral terraces. The red color corresponds to the 100 Kyr climatic cycle period, the yellow color corresponds to the ~40–60 Kyr climatic cycle period. The dashed red squares in Model b correspond to the missing level. Topographic profile n°8. The table to the right summarizes the main value of the tables in Figure S8 in Supporting Information S1. It presents the uplift rates obtained from the average elevation of the terraces and for the extreme scenario considering respectively the lowest (min) and highest (max) elevation for each terrace.

In terms of tectonic activity, however, it is difficult to explain why the tectonic vertical motion would slow down suddenly by a factor of 4, during a period where no major tectonic change is known in the area. However, this quick variation coincides with the change from a global ~30–60 Kyr glacial-interglacial cycle to a global ~70–120 Kyr glacial-interglacial cycle (Figures 3 and 4).

In this first model we assume that the recurrence time between two climatic cycles is sufficiently long to raise and isolate the marine terrace from the next MIS. However, in the case of shorter or stronger climatic cycles (maximum sea level higher or equal to the elevation of the previously-formed terrace), the possibility of remobilization or reoccupation of the previously-formed terraces cannot be ruled out. Hence, the absence of some terrace levels would lead to an overestimation of the uplift rate, thus the change of uplift rate in this model might be due to a bias in this age model.

In fact, in this area we would rather expect a low tectonic uplift rate, thus we need to consider that each level of terrace might not be necessarily well individualized and that gaps in the marine terrace record could exist. Building on this idea, we propose a second model (Figure 7b), in which we assume that the uplift rate should be constant through the last 5 Myr, the time of the last known event responsible for a significant change of the tectonic constraints along the DSF (Butler et al., 1998; Garfunkel et al., 1981; Joffe & Garfunkel, 1987; Lefevre, 2018). In this model, we also consider the possibility that some terraces might be missing and that the record is unlikely to be fully complete for the older terraces, although we try to minimize the number of missing terraces. Based on these assumptions, we determine an uplift rate from the first terrace levels (MIS 1 to MIS 17) according to the constant elevation difference between two successive levels (~20 m) and the climatic cycle variation (~100 Kyr). On the profile presented in Figure 7, the missing level associated with the MIS 19 corresponds to a lack of information at the surface of the island as the differential elevation between the terraces of the MIS 17 and MIS 21 is around 40 m, so twice as the measured differential elevation between the youngest MIS. We assume that the MIS 19 level is probably masked by thick slope deposits and is not visible on the satellite imagery. Then, to test the uplift rate derived from that model we predict the elevation of the upper fly of terraces and we check this prediction against our observations while keeping in mind that the terrace record is likely incomplete. The uplift rate that best adjusts the first terrace levels (MIS 1 to MIS 17) as well as best predicts the elevation of the upper terraces, without inflating the number of missing terraces, yields a value of 0.21 ± 0.02 mm/year. In this second model, the 19 levels preserved along Tiran Island register at least ~2.4 Myr of tectonic uplift (see Figure S9 in Supporting Information S1).

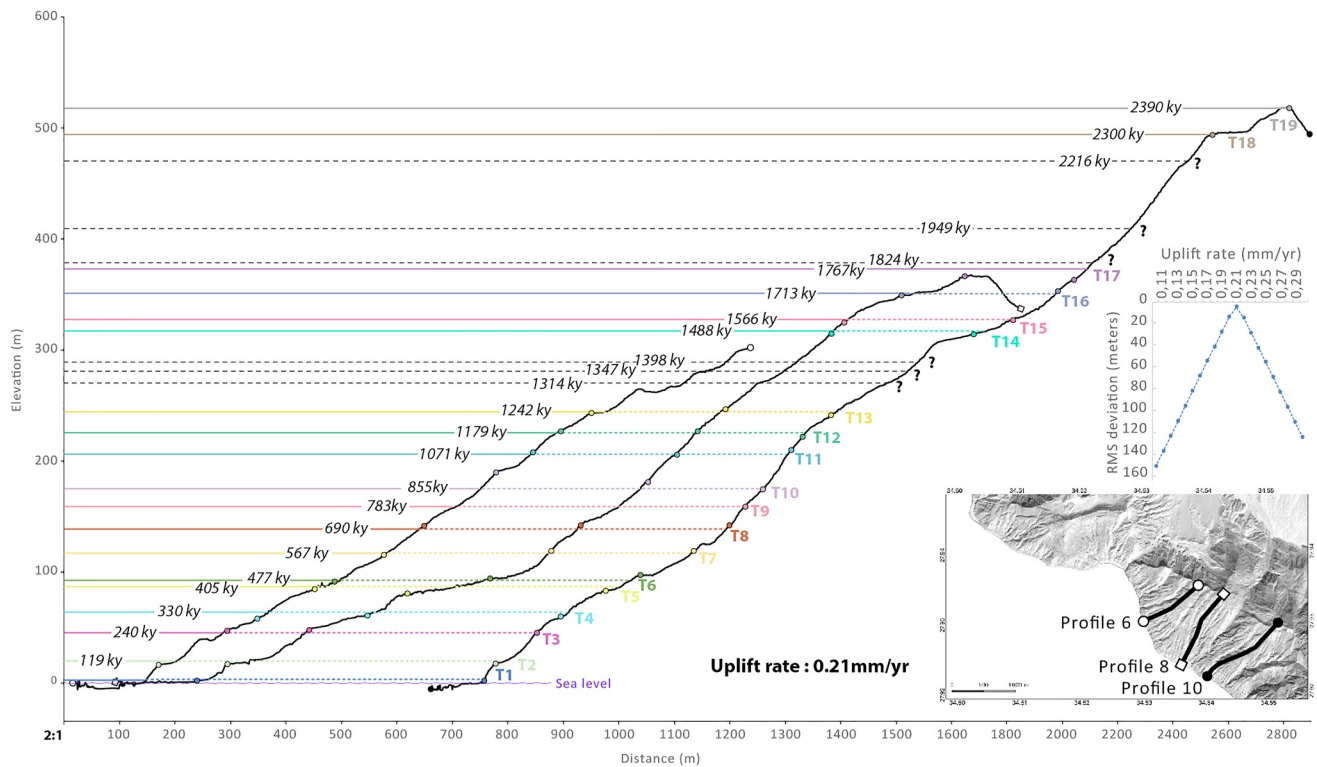


Figure 8. Best fit model using the synchronous correlation method on the terraces of Tiran Island. The topographic profiles ($Z_{\text{factor}} = 2$) are derived from our high-resolution Pleiades Digital Surface Model. The predicted paleo-shorelines (colored lines) fit with the elevation of the terraces (colored dots) within a confidence interval of ± 10 m. Extra levels (black dashed lines) could be inferred from the model and are consistent with the slope changes in topographic profiles. Root Mean Square (RMS) deviation is calculated using the misfit between the measured and expected elevation of the terraces. The smallest RMS (5 m) is minimized for an uplift rate of 0.21 mm/year.

This second model, even if we are still missing quite a large number of levels, allows us to obtain a solution that is both consistent with the regional tectonic history that suggests a constant uplift rate and with our observations. It also confirms our hypothesis that coupling a low tectonic uplift, here ~ 0.2 mm/year, with a short recurrence time of 40–60 Kyr induced by the climatic forcing, the terraces cannot be raised high enough to be systematically disconnected from the sea.

3.3. Validation of the Age Model

For the validation of our age model, we tested a synchronous correlation method on the terraces of Tiran Island. The synchronous correlation method (Houghton et al., 2003; Meschis et al., 2018, 2022; Roberts et al., 2009, 2013) is an iterative method to calculate the expected paleo-shoreline elevations for a given uplift rate, while accounting for the sea level variations. This synchronous approach includes all measured paleo-shoreline elevations correlated with all predicted paleo-shoreline elevations synchronously. To define the best-fit model that defines the uplift rate, we minimize the Root Mean Square (RMS) between the measured and calculated elevation of the terraces. To handle uncertainties due to age or elevation variation, we considered a confidence interval of ± 10 m between the measured and expected backpoint elevations. We tried a range of uplift values, from 0.1 to 0.3 mm/year, with a successive step of 0.01 mm/year separately over several profiles located on the southwestern part of the island. The uplift rate that minimizes the RMS is 0.21 mm/year (Figure 8) for the terraces along profiles 6, 8, and 10 on Tiran Island. This uplift rate, considering only the paleo-record of the island with an imposed tectonic uplift, correlates with the tectonic uplift derived from our age model. In addition, it confirms the assumptions made on the second model, of missing terrace levels in the higher part of the island to explain a constant uplift rate throughout the last 2.4 Myr. Moreover, the synchronous correlation model also emphasizes the presence of additional levels, not visible at the surface because they are covered by thick slope deposits, but that can still be inferred along the topographic profiles (see Figure 8). The paleo-elevations deduced from the

synchronous correlation model fit with the slope breaks visible on the topographic profiles 6, 8, and 10 (see Figure 8) and suggest the existence of 6 additional levels to the 19 levels already mapped on the island.

3.4. The Uplift Rate of the Coral Terraces From the Gulf of Aqaba to Tiran Island

In the Gulf of Aqaba, once the eustatic variations are accounted for, the tectonic activity of the faults located on-land (Lefevre, 2018) and off-shore (Ben-Avraham et al., 1979; Ribot et al., 2021) yield an uplift rate between 0.1 and 0.2 mm/year for the terraces, according to earlier results (Barnea et al., 2015; Bosworth et al., 2017; Gvirtzman et al., 1992; Lazar & Stein, 2011; Manaa et al., 2016; Weil, 2008; Yehudai et al., 2017). In details, on the seven sites where we have collected coral samples, we defined an uplift rate of 0.14 ± 0.01 mm/year at Al Humidah, 0.14 ± 0.03 mm/year at Alwasel, 0.14 ± 0.02 mm/year at Ash Shurayh North, 0.14 ± 0.03 mm/year at Mountain Range, 0.14 ± 0.03 mm/year at North magna, 0.14 ± 0.02 mm/year at Magna, and 0.15 ± 0.03 mm/year at Ras Alsheikh Hamid (see localization on Figure 5, ages and elevation data are presented in Figure S10 in Supporting Information S1). In the south, at Ras Alsheikh Hamid, our estimation of the uplift rate differs from the rate from Bosworth et al. (2017), and we think it is due to the particular geometry of the Midyan area. Indeed, the relatively flat area allows a complete development of the marine terraces (see Figure 2) and then the preservation of both the FR and the RF. Bosworth et al. (2017) obtained an age of 120 Kyr at 8.73 ± 0.24 m. In the same area we obtained similar ages for samples at elevations varying from 3 to 21 m (see samples Aq22 in Tables 1 and 2) which suggest that they might have sampled the FR. As we estimate the uplift using the elevation of the RF and not of the FR, it would explain the differences.

Along the southeastern part of Sinai, close to Sharm el-Sheikh and Ras Mohamed, Gvirtzman (1994) evidenced the presence of uplifted terraces. Four distinct reefs, gave respectively ages of 5.2 Kyr (MIS 1.1), 122 Kyr (MIS 5e), 206 Kyr (MIS 7a), and 310 Kyr (MIS 9c). The authors assumed a correlation of these reefs with the Milankovitch cycles (120 Kyr) and estimated an uplift rate of 0.085 mm/year.

On Tiran Island, Goldberg and Yaron (1978) assigned an age of 146 ± 16 Kyr for the reef that is at 40 m above the MSL on the island. Goldberg and Beyth (1991) refined this value and reported this age to be close to 130 Kyr, and possibly part of the MIS 5e terrace. They also report the uplift of the island to be close to 0.3 mm/year. We slightly refine the age to the MIS 5e terrace around 119 Kyr and be part of level T2, which ranges in an elevation close to 25 m amsl. After correction of the eustatic variation, the uplift rate is close to 0.25 mm/year and it agrees with the uplift rate deduced from our age model, where we estimate a mean uplift rate for Tiran Island of 0.21 ± 0.02 mm/year.

To summarize, along the Gulf of Aqaba and in the Strait of Tiran, several levels of terraces are identified as marine terraces uplifted by tectonic activity related to the DSF system (Bar et al., 2018; Bosworth et al., 2017; Manaa et al., 2016; Taviani et al., 2019; Yehudai et al., 2017). The coral terraces are exposed between 1 m and more than 500 m above the MSL (Dullo, 1990; El-Asmar, 1997; Friedman, 1965; Goldberg & Beyth, 1991; Goldberg & Yaron, 1978; Gvirtzman, 1994; Moustafa et al., 2000; Parker et al., 2012; Schick, 1958). Studies of the marine terraces located in the gulf and the strait of Tiran suggest that the uplift of these terraces ranges between 0.08 and 0.2 mm/year.

4. Discussion

4.1. Tectonic Evolution of the Tiran Island

Described in the 1980s as a tilted block (Goldberg & Yaron, 1978), Tiran Island is an uplifted structure resulting from the combined activities of the Dead Sea strike-slip fault system and of the opening Red Sea rift. Goldberg and Beyth (1991) proposed that the tectonic uplift of the island started between 1.7 and 2.5 Myr, which is consistent with our reassessment of the age of the uppermost terraces at the top of Tiran Island of about 2.4 Myr. However, the initiation of the uplift of the Tiran block must have started earlier as the Tiran block was initially submerged and coral terraces can only date the beginning of the emergence of the island. Around 5 Myr ago, several major changes are documented that affect the regional tectonic framework, such as the migration of the Arabia-Nubia Euler pole (Garfunkel, 1981; Le Pichon & Gaulier, 1988), the intensification of the strike-slip motion along the southern Dead Sea strike-slip system (Ehrhardt et al., 2005), the beginning of the main subsidence in the Dead Sea basin and the formation of the Sea of Galilee and the Hula Basin to the north along the DSF system (Garfunkel & Ben-avraham, 2001), the initiation of active seafloor spreading in the southern Red Sea

(Roesser, 1975), and evidence of vertical motions in the Midyan basin ($28^{\circ}13'48''$, $34^{\circ}57'17''$) at the beginning of the Pliocene (Tubbs et al., 2014). Thus, although we have no way to determine with more accuracy the beginning of the Tiran Island uplift, several lines of evidence suggest that it is likely around 5 Myr, concomitant with all major changes in the area, even if we cannot rule out that a previous uplift event might have occurred in the surrounding of the island, in particular when Tiran Island was closer to the Suez rift system.

Furthermore, if we consider a constant uplift rate close to 0.21 ± 0.02 mm/year since 5 Myr, the total uplift of the Tiran block should be around $1,050 \pm 100$ m. Based on the classical distribution of motion along normal faults (1/3 of uplift for the footwall and 2/3 of subsidence for the hanging wall (Martel et al., 2014)), if the Tiran block, which stands on the footwall, accommodated $1,050 \pm 100$ m of uplift in 5 Myr, the total offset between the hanging wall and the footwall should be around $3,150 \pm 300$ m. Today, the top of Tiran Island is around 500 m above sea level and the depth of the sediment-covered top of the hanging wall in the Hume Deep is around 1,400 m below sea level. The only available seismic line in the area (seismic line 6ii in Ben-Avraham, 1985) suggests sediment infill thickness that is at least 1,100 m, possibly $\sim 1,700$ m, although this is poorly constrained. This would lead to a differential elevation between the bottom of the basin and the top of the Tiran block of about 3,000–3,600 m, consistent with an uplift rate of 0.21 ± 0.02 mm/year over 5 Myr.

4.2. The Strike-Slip Tiran Fault and the Normal Hume Fault

Tiran Island is located at the junction between two fault systems: To the north is the strike-slip DSF, and to the south-east is the extensional Red Sea fault system. Thus, it is expected that the deformation documented by the uplifted coral terraces would reflect the kinematics of those two systems.

In the direct vicinity of Tiran Island (Figure 1b), one can see in the bathymetric data the Tiran strike-slip fault, which is the southern continuation of the DSF, and, on the other hand, the main normal Hume fault, which is located at the toe of the western shore of Tiran Island. The global geometry of Tiran Island, with uplifted terraces mostly located on the southern shore, emphasizes that the uplift of the island is primarily controlled by the Hume fault off-shore. The orientation of the normal Hume fault ($N160^{\circ}E$) aligns both with the orientation of the normal faults trending $N160^{\circ}E$ in the Gulf of Aqaba (Ribot et al., 2021), and with the orientation of the normal faults related to Red Sea rift system, whose strike ranges between $N140^{\circ}E$ and $N160^{\circ}E$. Hence, it can be argued whether the Hume fault is part either of the Red Sea system or of the DSF system. The latter implies that it would be an additional pull-apart basin associated with the DSF mostly filled by salt, with the Hume Deep and Sharm Deep the remaining visible parts of this basin. The bathymetry of the area shows that these two deeps have a similar depth (see Figure 1), comparable to the one of the Tiran and Dakar deeps inside the Gulf of Aqaba (Ribot et al., 2021). Moreover, they are flat narrow areas with steep well delineated borders, quite at odd with the morphology of the other basins visible in the northern Red Sea (see Figure 1). Thus, it suggests that those basins might rather be associated with the DSF system, and probably correspond to a single basin with its central part filled by salt sliding from the neighboring plateau, as it has been observed further north around the Dahab plateau (Ribot et al., 2021). This implies that the Tiran strike-slip fault, bounding the western side of the Hume Deep and Sharm Deep (see Figure 1), is not the last en-echelon fault of the DSF system, but that at least one extra strike-slip fault section, belonging to the DSF system has to exist, east of the Hume Deep, and is currently hidden under the salt body gliding into the Hume Deep. Such geometry is consistent with the recent reconstruction of the Red Sea opening from Delaunay et al. (2023), where they accommodate part of the deformation along a transverse structure that would correspond to the hidden fault we propose. Moreover, in the gravity anomaly data (Delaunay et al., 2023), we can see that at this location there is an abrupt change of gravity value that supports the presence of another echelon of the DSF eastward of the Tiran fault. Finally, such geometry would also explain the morphology of the western border of the Sharm deep; In the bathymetry, it is clear that in the Sharm deep the Tiran fault does not continue straight to the south, and then it could correspond to the end of this echelon, or highlight the presence of a small relay to the west crossing the Ras Muhammad peninsula. Thus, based on these observations we propose that even if the Hume fault might be inherited from an old extensive episode of the Red Sea, currently it corresponds to an active normal fault bounding the southernmost pull-apart basin of the DSF. Therefore, we expect that most of the deformation accommodated along this fault reflects the activity of the DSF.

The different uplift rates we obtained with the terraces of Tiran Island tend to confirm that at the present time the Hume fault is part of the DSF system. Indeed, on Tiran Island we find in the southern part an uplift of 0.21 ± 0.02 mm/year since at least 1 Ma. In parallel, several studies of the Pleistocene marine terraces uplifted

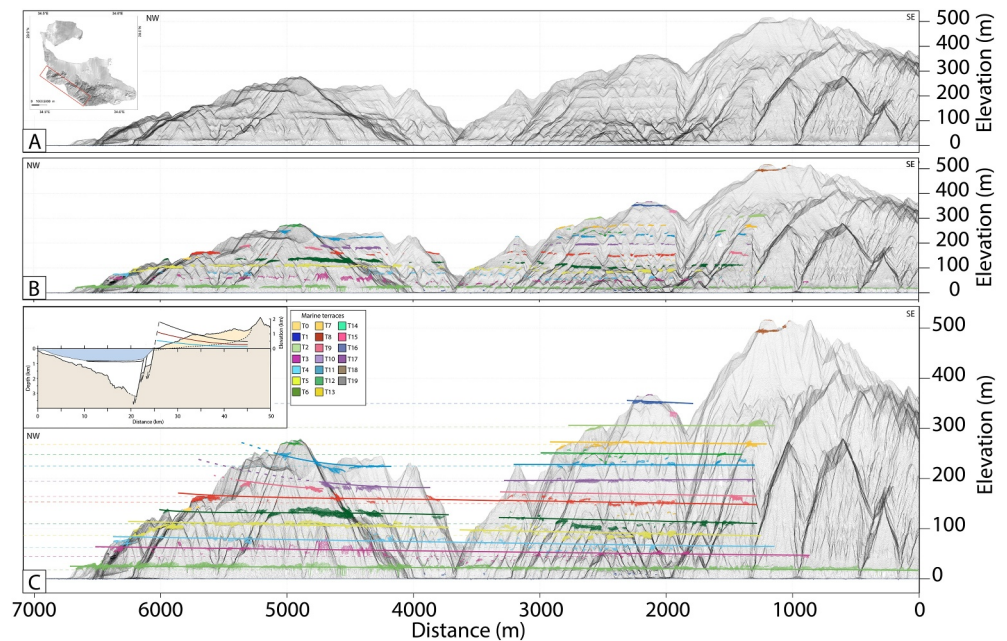


Figure 9. (a) Transverse view of the southwestern part of Tiran Island derived from stack swath profiles ($Z_{\text{factor}} = 2$). (b) Mapped marine terraces plotted on the stack swath profiles. They present a slight tilt toward the SE. (c) The tilt of the marine terraces is clearer when the vertical exaggeration is increased ($Z_{\text{factor}} = 8$), indicating differential uplift of the island. The solid lines represent the average shape of the terraces along the island to help the visualization, the dashed colored lines represent the lateral continuity of the terraces considering the same uplift rate all along the island. The inset in the top left corner is a schematic view of the lithospheric flexure generated by the fault activity, modified from de Gelder et al. (2019).

along the Red Sea rift reveal a low tectonic activity with an uplift rate ranging between 0.02 mm/year for the central Red Sea, and 0.08 mm/year for the northern Red Sea coast during the last 200 Kyr. In detail, in the southern part of the Red Sea, at latitudes between 13°N and 22°N, uplifted coral terraces at 2–3 m were dated to be 135 Kyr old (Brown et al., 1989). To the north, at Rabigh (22°47'34", 39°02'01"), uplifted terraces at 2.5–3.3 m amsl, yield an age of 212–235 Kyr (Dawood et al., 2013). Further north, near Duba (27°33'15", 35°32'04"), coral terraces between 6 and 10 m amsl have been dated around 95–120 Kyr (Jado et al., 1989). Thus, assuming that a part of the tectonic uplift in Tiran Island is related to the Red Sea system and considering a maximum uplift rate of 0.08 mm/year for that component of motion, there is still an uplift rate of 0.13 ± 0.04 mm/year along the Hume fault to explain. The uplifted terraces along the Gulf of Aqaba show that on average the uplift of the western coast associated to the deformation along the DSF system is of the order of 0.14 ± 0.03 mm/year, which is in good agreement with the remaining deformation observed on the Hume fault after retrieving the Red Sea component.

We also observed on Tiran Island a tilt of the terraces toward the east, suggesting a higher uplift in the western part of the island (see Figure 9). West of Tiran another fault is present, the Tiran strike-slip fault, thus considering the coral terraces as a benchmark of the sea level along the island, the fan shape (Figure 9c) of the terraces, as well as the general decrease of the elevation toward the east of the Level 2, 5, and 6 of respectively, ~10, ~33 and ~33 m, underline that the part of the uplift generated by the Tiran fault is non-negligible. We extracted the elevation of the terraces located in the west of the island and, with the synchronous age model, we estimate an uplift rate of 0.25 ± 0.02 mm/year (see Figure S11 in Supporting Information S1). We propose that the difference between the uplift rates determined respectively in the west and the southwest of the island (i.e., 0.25 ± 0.02 mm/year and 0.21 ± 0.02 mm/year) corresponds to the part of the uplift generated by the activity of the Tiran strike-slip fault, that is registered only in the areas close to the fault. The magnitude of this uplift variation corresponds to what can be observed along the gulf, depending on the distance of the main faults, which confirms this hypothesis.

5. Conclusions

This work constrains the vertical uplift along the eastern coast of the Gulf of Aqaba—Tiran Island system during the last 500 Kyr. Based on a series of markers distributed along strike in the gulf, the uplift rate is estimated to be

about 0.14 ± 0.03 mm/year all over the gulf. This uplift is associated with secondary extension and strike-slip faulting along the DSF system. The southern termination of the strike-slip fault system, marked by Tiran Island, seems to be affected by the Red Sea rift system as the uplift rate deduced on the island is a combination of the rates defined along the Red Sea and the Gulf of Aqaba coral terraces. Previous work suggested that the uplift of Tiran Island initiated back to 2.4 Myr. However, considering the elevation of the terraces documented on Tiran Island we suggest that the total vertical motion is about 3,600 m. With a total uplift rate for Tiran Island of ~ 0.20 mm/year, thus it would rather imply initiating vertical motion at 5 Myr, which is consistent with a major regional tectonic reorganization also documented otherwise.

Eventually, Tiran Island is uplifted by the normal fault separating the island from the Hume Deep, while the tilt toward the east of Tiran Island results from the activity of the Tiran fault. The geometry of the faults and the differential uplift of the island pushes forward the idea that the Hume fault is still associated with the DSF system. Therefore, further en-echelon strike-slip faults in the northern Red Sea, already covered by thick salt deposits flowing from the continent, need to be considered to point out the location of the Red-Sea-Gulf of Suez-Gulf of Aqaba triple junction.

Data Availability Statement

Bathymetric data are available from Ribot et al. (2024). Bathymetric data from the Northern Red Sea [Dataset]. Zenodo. <https://doi.org/10.5281/zenodo.11610050>.

Pleiades' satellite imagery was obtained through the ISIS program of the CNES under an academic license and is not for open distribution. On request, we will provide the DSM calculated from this imagery to any academic researcher who gets approval from CNES (contact isis-pleiades@cnes.fr quoting this paper, klinger@ippg.fr in copy).

Additional data can be found in Supporting Information S1.

Acknowledgments

This study was funded by King Abdullah University of Science and Technology (KAUST), under award numbers OSR-2016-CRG5-3027-01 and OSR-CRG2020-4335. We thank Rodrigo Pulahinge (CMOR, KAUST) for the help with the multibeam data acquisition and initial processing, and the crew on the R/V Thuwal for their work during the September 2019 research cruise. We are very grateful to Serge Miska (GEOPS, France) for the help in DRX data acquisition. We thank Lorna Foliot (LSCE) for her help in the acquisition of the U-Th data, Arthur Delorme for assistance in producing the DSM, Marco Meschis for the fruitful discussions about the synchronous correlation technique, and Adriano Nobile for the help with coding. Numerical computation was performed on the S-CAPAD platform at Institut de Physique du Globe de Paris (IPGP, France). Finally, we would like to thank William Bosworth and one anonymous reviewer for their constructive reviews that helped significantly improve the quality of our manuscript.

References

- Alamri, A. M., Schult, F. R., & Bufer, C. G. (1991). Seismicity and aeromagnetic features of the Gulf of Aqaba (Elat) Region. *Journal of Geophysical Research*, 96(B12), 20179–20185. <https://doi.org/10.1029/91JB02104>
- Al-Rifa'i, I. A., & Cherif, O. H. (1988). The fossil coral reefs of al-Aqaba, Jordan. *Facies*, 18(1), 219–229. <https://doi.org/10.1007/BF02536801>
- al Tarazi, E., Abu Rajab, J., Gomez, F., Cochran, W., Jaafar, R., & Ferry, M. (2011). GPS measurements of near-field deformation along the southern Dead Sea Fault System. *Geochemistry, Geophysics, Geosystems*, 12, Q12021. <https://doi.org/10.1029/2011GC003736>
- Anderson, R. S., Densmore, A. L., & Ellis, M. A. (1999). The generation and degradation of marine terraces. *Basin Research*, 11(1), 7–20. <https://doi.org/10.1046/j.1365-2117.1999.00085.x>
- Armijo, R., Meyer, B., King, G. C. P., Rigo, A., & Papanastasiou, D. (1996). Quaternary evolution of the Corinth Rift and its implications for the Late Cenozoic evolution of the Aegean. *Geophysical Journal International*, 126(1), 11–53. <https://doi.org/10.1111/j.1365-246X.1996.tb05264.x>
- Badawy, A., & Horváth, F. (1999). Recent stress field of the Sinai subplate region. *Tectonophysics*, 304(4), 385–403. [https://doi.org/10.1016/S0040-1951\(98\)00271-6](https://doi.org/10.1016/S0040-1951(98)00271-6)
- Bantan, R. A., Abu-Zied, R. H., & Haredy, R. A. (2015). Lithology, fauna and environmental conditions of the Late Pleistocene raised reefal limestone of the Jeddah coastal plain, Saudi Arabia. *Arabian Journal of Geosciences*, 8(11), 9887–9904. <https://doi.org/10.1007/s12517-015-1884-6>
- Bar, N., Agnon, A., Yehudai, M., Lazar, B., Shaked, Y., & Stein, M. (2018). Last interglacial sea levels and regional tectonics from fossil coral reefs in the northeast Gulf of Aqaba. *Quaternary Science Reviews*, 191, 41–56. <https://doi.org/10.1016/j.quascirev.2018.04.031>
- Bard, E., Hamelin, B., & Fairbanks, R. G. (1990). U/Th ages obtained by mass spectrometry in corals from Barbados. *Chemical Geology*, 84(1–4), 157–158. [https://doi.org/10.1016/0009-2541\(90\)90196-E](https://doi.org/10.1016/0009-2541(90)90196-E)
- Bar-Matthews, M., Wasserburg, G. J., & Chen, J. H. (1993). Diagenesis of fossil coral skeletons: Correlation between trace elements, textures, and $^{234}\text{U}/^{238}\text{U}$. *Geochimica et Cosmochimica Acta*, 57(2), 257–276. [https://doi.org/10.1016/0016-7037\(93\)90429-Z](https://doi.org/10.1016/0016-7037(93)90429-Z)
- Barnea, O., Stein, M., Shaked, Y., & Agnon, A. (2015). Radiocarbon and U-Th dating of Holocene reefs from the northern Gulf of Aqaba: Implications for sea-levels, tectonics and reservoir ages. In *Goldschmidt abstract*.
- Bartov, Y., Steinitz, G., Eyal, M., & Eyal, Y. (1980). Sinistral movement along the Gulf of Aqaba - Its age and relation to the opening of the Red Sea. *Nature*, 285(5762), 220–222. <https://doi.org/10.1038/285220a0>
- Bates, S. L., Siddall, M., & Waelbroeck, C. (2014). Hydrographic variations in deep ocean temperature over the mid-Pleistocene transition. *Quaternary Science Reviews*, 88, 147–158. <https://doi.org/10.1016/j.quascirev.2014.01.020>
- Bayer, H. J., Hötzl, H., Jado, A. R., Röscher, B., & Voggenreiter, W. (1988). Sedimentary and structural evolution of the northwest Arabian Red Sea margin. *Tectonophysics*, 153(1–4), 137–151. [https://doi.org/10.1016/0040-1951\(88\)90011-X](https://doi.org/10.1016/0040-1951(88)90011-X)
- Ben-Avraham, Z. (1985). Structural framework of the Gulf of Elat (AQABA), Northern Red Sea. *Journal of Geophysical Research*, 90(B1), 703–726. <https://doi.org/10.1029/JB090iB01p00703>
- Ben-Avraham, Z., Almagor, G., & Garfunkel, Z. (1979). Sediments and structure of the Gulf of Elat (Aqaba)-Northern Red Sea. *Sedimentary Geology*, 23(1–4), 239–267. [https://doi.org/10.1016/0037-0738\(79\)90016-2](https://doi.org/10.1016/0037-0738(79)90016-2)
- Ben-Avraham, Z., & Zoback, M. D. (1992). Transform-normal extension and asymmetric basins: An alternative to pull-apart models. *Geology*, 20(5), 423–426. [https://doi.org/10.1130/0091-7613\(1992\)020<0423:tneab>2.3.co;2](https://doi.org/10.1130/0091-7613(1992)020<0423:tneab>2.3.co;2)

- Bosworth, W., & Burke, K. (2005). Evolution of the Red Sea—Gulf of Aden Rift System. In *Petroleum systems of divergent continental margin basins: 25th annual* (pp. 342–372). <https://doi.org/10.5724/gcs.05.25.0342>
- Bosworth, W., Montagna, P., Pons-Branchu, E., Rasul, N., & Taviani, M. (2017). Seismic Hazards implications of uplifted pleistocene coral terraces in the Gulf of Aqaba. *Scientific Reports*, 7, 1–13. <https://doi.org/10.1038/s41598-017-00074-2>
- Bott, M. H. (1997). Modeling the formation of a half graben using realistic upper crustal rheology. *Journal of Geophysical Research*, 102(B11), 24605–24617. <https://doi.org/10.1029/97jb02124>
- Brown, G. F., Schmidt, D. L., & Huffman, A. C. (1989). Geology of the Arabian Peninsula: Shield area of western Saudi Arabia. 560 A. <https://doi.org/10.3133/pp560A>
- Butler, R. W. H., Spencer, S., & Griffiths, H. M. (1998). The structural response to evolving plate kinematics during transpression: Evolution of the Lebanese restraining bend of the Dead Sea Transform. *Geological Society, London, Special Publications*, 135(1), 81–106. <https://doi.org/10.1144/GSL.SP.1998.135.01.06>
- Castro-Perdomo, N., Viltres, R., Masson, F., Klinger, Y., Liu, S., Dhahry, M., et al. (2022). Interseismic deformation in the Gulf of Aqaba from GPS measurements. *Geophysical Journal International*, 228(1), 477–492. <https://doi.org/10.1093/gji/ggab353>
- Chappell, J. (1974). Geology of coral terraces, Huon Peninsula, New Guinea: A study of Quaternary tectonic movements and sea-level changes. *Geological Society of America Bulletin*, 85(4), 553–570. [https://doi.org/10.1130/0016-7606\(1974\)85<553:gocthp>2.0.co;2](https://doi.org/10.1130/0016-7606(1974)85<553:gocthp>2.0.co;2)
- Cheng, H., Lawrence Edwards, R., Shen, C., Polyak, V., Asmerom, Y., Woodhead, J., et al. (2013). Improvements in ^{230}Th dating, ^{230}Th and ^{234}U half-life values, and U-Th isotopic measurements by multi-collector inductively coupled plasma mass spectrometry. *Earth and Planetary Science Letters*, 371–372, 82–91. <https://doi.org/10.1016/j.epsl.2013.04.006>
- Chutcharavan, P. M., Dutton, A., & Ellwood, M. J. (2018). Seawater $^{234}\text{U}/^{238}\text{U}$ recorded by modern and fossil corals. *Geochimica et Cosmochimica Acta*, 224, 1–17. <https://doi.org/10.1016/j.gca.2017.12.017>
- Courtillot, V., Armijo, R., & Tapponnier, P. (1987). The Sinai triple junction revisited. *Tectonophysics*, 141(1–3), 181–190. [https://doi.org/10.1016/0040-1951\(87\)90184-3](https://doi.org/10.1016/0040-1951(87)90184-3)
- Daëron, M., Benedetti, L., Tapponnier, P., Surssock, A., & Finkel, R. C. (2004). Constraints on the post ~25-ka slip rate of the Yammouneh fault (Lebanon) using in situ cosmogenic ^{36}Cl dating of offset limestone-clast fans. *Earth and Planetary Science Letters*, 227(1–2), 105–119. <https://doi.org/10.1016/j.epsl.2004.07.014>
- Davison, I., Al-Kadasi, M., Al-Khirbash, S., Al-Subbary, A. K., Baker, J., Blakey, S., et al. (1994). Geological evolution of the southeastern Red Sea Rift margin, Republic of Yemen. *Geological Society of America Bulletin*, 106(11), 1474–1493. [https://doi.org/10.1130/0016-7606\(1994\)106<1474:geotsr>2.3.co;2](https://doi.org/10.1130/0016-7606(1994)106<1474:geotsr>2.3.co;2)
- Dawood, Y. H., Aref, M. A., Mandurah, M. H., Hakami, A., & Gameil, M. (2013). Isotope geochemistry of the Miocene and Quaternary carbonate rocks in Rabigh area, Red Sea coast, Saudi Arabia. *Journal of Asian Earth Sciences*, 77, 151–162. <https://doi.org/10.1016/j.jseaeas.2013.08.031>
- de Gelder, G., Fernández-Blanco, D., Melnick, D., Duclaux, G., Bell, R. E., Jara-Muñoz, J., et al. (2019). Lithospheric flexure and rheology determined by climate cycle markers in the Corinth Rift. *Scientific Reports*, 9, 1–12. <https://doi.org/10.1038/s41598-018-36377-1>
- de Gelder, G., Jara-Muñoz, J., Melnick, D., Fernández-Blanco, D., Rouby, H., Podoja, K., et al. (2020). How do sea-level curves influence modeled marine terrace sequences? *Quaternary Science Reviews*, 229, 106132. <https://doi.org/10.1016/j.quascirev.2019.106132>
- Delaunay, A., Baby, G., Alafifi, A., Fedorik, J., Dymant, J., & Tapponnier, P. (2023). Structure and morphology of the Red Sea. From the Mid-Ocean Ridge to the Ocean-Continent Boundary. *SSRN Electronic Journal*, 849. <https://doi.org/10.2139/ssrn.4246850>
- Dullo, W. (1990). Facies, Fossil Record, and Age of Pleistocene Reefs from the Red Sea (Saudi Arabia) Fazies, FossilOberlieferung und Alter der pleistoz & nen Rifle am Roten Meer (Saudi Arabien). *Facies*, 22, 1–45. <https://doi.org/10.1007/BF02536943>
- Ehrhardt, A., Hübscher, C., Ben-Avraham, Z., & Gajewski, D. (2005). Seismic study of pull-apart-induced sedimentation and deformation in the Northern Gulf of Aqaba (Elat). *Tectonophysics*, 396(1–2), 59–79. <https://doi.org/10.1016/j.tecto.2004.10.011>
- El-Asmar, H. M. (1997). Quaternary isotope stratigraphy and paleoclimate of coral reef terraces, Gulf of Aqaba, south Sinai, Egypt. *Quaternary Science Reviews*, 16(8), 911–924. [https://doi.org/10.1016/S0277-3791\(96\)00077-7](https://doi.org/10.1016/S0277-3791(96)00077-7)
- Elias, A., Tapponnier, P., Singh, S. C., King, G. C. P., Briaes, A., Daëron, M., et al. (2007). Active thrusting offshore Mount Lebanon: Source of the tsunamigenic AD 551 Beirut-Tripoli earthquake. *Geology*, 35(8), 755–758. <https://doi.org/10.1130/G23631A.1>
- Elias, A., Tapponnier, P., Surssock, A., Daëron, M., Jacques, E., & King, G. (2007). Mid-Miocene to present growth and uplift of Mt-Lebanon and tectonic evolution of the Dead Sea Transform's Restraining Bend. In *AGU fall meeting abstracts* (Vol. 2007, pp. T43A-1091).
- Freund, A. R., Garfunkel, Z., Zak, I., Goldberg, M., Weissbrod, T., Derin, B., et al. (1970). The shear along the Dead Sea rift. *Philosophical Transactions of the Royal Society of London A: Mathematical, Physical and Engineering Sciences*, 267, 107–130.
- Friedman, G. M. (1965). A fossil shoreline reef in the Gulf of Elat (Aqaba). *Israel Journal of Earth Sciences*, 14, 86–90.
- Friedman, G. M. (1968). Geology and geochemistry of reefs, carbonate sediments, and waters, Gulf of Aqaba (Elat), Red Sea. *Journal of Sedimentary Research*, 38, 895–919. <https://doi.org/10.1306/74d71aaa-2b21-11d7-8648000102c1865d>
- Gabrie, C., & Montaggioni, L. (1982). Sedimentary facies from the modern coral reefs, Jordan Gulf of Aqaba, Red Sea. *Coral Reefs*, 1(2), 115–124. <https://doi.org/10.1007/bf00301693>
- Garfunkel, Z. (1981). Internal structure of the Dead Sea leaky transform (rift) in relation to plate kinematics. *Tectonophysics*, 80(1–4), 81–108. [https://doi.org/10.1016/0040-1951\(81\)90143-8](https://doi.org/10.1016/0040-1951(81)90143-8)
- Garfunkel, Z., & Ben-avraham, Z. (2001). Basins along the Dead Sea transform. *Mémoires du Muséum National d'histoire Naturelle (1993)*, 186, 607–627.
- Garfunkel, Z., & Beyth, M. (2006). Constraints on the structural development of Afar imposed by the kinematics of the major surrounding plates. *Geological Society Special Publication*, 259(1), 23–42. <https://doi.org/10.1144/GSL.SP.2006.259.01.04>
- Garfunkel, Z., Ginzburg, A., & Searle, R. C. (1987). Fault pattern and mechanism of crustal spreading along the axis of the Red Sea from side scan sonar (GLORIA) data. *Annales Geophysicae. Series B. Terrestrial and Planetary Physics*, 5, 187–200.
- Garfunkel, Z., Zak, I., & Freund, R. (1981). Active faulting in the Dead Sea Rift. *Tectonophysics*, 80(1–4), 1–26. [https://doi.org/10.1016/0040-1951\(81\)90139-6](https://doi.org/10.1016/0040-1951(81)90139-6)
- Goldberg, M., & Beyth, M. (1991). Tiran Island: An internal block at the junction of the Red Sea rift and Dead Sea transform. *Tectonophysics*, 198(2–4), 261–273. [https://doi.org/10.1016/0040-1951\(91\)90154-K](https://doi.org/10.1016/0040-1951(91)90154-K)
- Goldberg, M., & Yaron, F. (1978). $\text{Th}^{230}/\text{U}^{234}$ Ages of raised pleistocene marine terraces on the island of Tiran and the southeastern coast of Sinai with some tectonic implications. In *IAS 10th Int. Congr. Sedimentology, Jerusalem* (pp. 258–259).
- Gomez, F., Karam, G., Khawlie, M., McClusky, S., Vernant, P., Reilinger, R., et al. (2007). Global Positioning System measurements of strain accumulation and slip transfer through the restraining bend along the Dead Sea fault system in Lebanon. *Geophysical Journal International*, 168(3), 1021–1028. <https://doi.org/10.1111/j.1365-246X.2006.03328.x>
- Goren, L., Castellort, S., & Klinger, Y. (2015). Modes and rates of horizontal deformation from rotated river basins: Application to the Dead Sea fault system in Lebanon. *Geology*, 43(9), 843–846. <https://doi.org/10.1130/G36841.1>

- Grant, K., Hemleben, C., Hoogakker, B. A. A., Rohling, E. J., Grant, K., Hemleben, C., et al. (2007). High rates of sea-level rise during the last interglacial period. *Nature Geoscience*, *1*, 38–42. <https://doi.org/10.1038/ngeo.2007.28>
- Gvirtzman, G. (1994). Fluctuations of sea level during the past 400 000 years: The record of Sinai, Egypt (northern Red Sea). *Coral Reefs*, *13*(4), 203–214. <https://doi.org/10.1007/BF00303633>
- Gvirtzman, G., Kronfeld, J., & Buchbinder, B. (1992). Dated coral reefs of southern Sinai (Red Sea) and their implication to late Quaternary sea levels. *Marine Geology*, *108*(1), 29–37. [https://doi.org/10.1016/0025-3227\(92\)90211-Y](https://doi.org/10.1016/0025-3227(92)90211-Y)
- Hamelin, B., Bard, E., Zindler, A., & Fairbanks, R. G. (1991). $^{234}\text{U}/^{238}\text{U}$ mass spectrometry of corals: How accurate is the UTh age of the last interglacial period? *Earth and Planetary Science Letters*, *106*(1–4), 169–180. [https://doi.org/10.1016/0012-821X\(91\)90070-X](https://doi.org/10.1016/0012-821X(91)90070-X)
- Hamiel, Y., Masson, F., Piatibratova, O., & Mizrahi, Y. (2018). GPS measurements of crustal deformation across the southern Arava Valley section of the Dead Sea Fault and implications to regional seismic hazard assessment. *Tectonophysics*, *724–725*, 171–178. <https://doi.org/10.1016/j.tecto.2018.01.016>
- Houghton, S. L., Roberts, G. P., Papanikolaou, I. D., McArthur, J. M., & Gilmour, M. A. (2003). New $^{234}\text{U}/^{238}\text{U}$ coral dates from the western Gulf of Corinth: Implications for extensional tectonics. *Geophysical Research Letters*, *30*(19), 3–6. <https://doi.org/10.1029/2003GL018112>
- Hughes, G. W., Varol, O., & Beydoun, Z. R. (1991). Evidence for Middle Oligocene rifting of the Gulf of Aden and for Late Oligocene rifting of the southern Red Sea. *Marine and Petroleum Geology*, *8*(3), 354–358. [https://doi.org/10.1016/0264-8172\(91\)90088-i](https://doi.org/10.1016/0264-8172(91)90088-i)
- Husson, L., Pastier, A. M., Pedoja, K., Elliot, M., Paillard, D., Authemayou, C., et al. (2018). Reef carbonate productivity during quaternary sea level oscillations. *Geochemistry, Geophysics, Geosystems*, *19*(4), 1148–1164. <https://doi.org/10.1002/2017GC007335>
- Jado, A. R., Hötzl, H., & Roscher, B. (1989). Development of sedimentation along the Saudi Arabian Red Sea coast. In *Saudi symposium on Earth Sciences*.
- Jaffey, A. H., Flynn, K. F., Glendenin, L. E., Bentley, W. C., & Essling, A. M. (1971). Precision measurement of half-lives and specific activities of U^{235} and U^{238} . *Physical Review C*, *4*(5), 1889–1906. <https://doi.org/10.1103/PhysRevC.4.1889>
- Joffe, S., & Garfunkel, Z. (1987). Plate kinematics of the circum Red Sea - A re-evaluation. *Tectonophysics*, *141*(1–3), 5–22. [https://doi.org/10.1016/0040-1951\(87\)90171-5](https://doi.org/10.1016/0040-1951(87)90171-5)
- Kennedy, D. M., & Woodroffe, C. D. (2002). Fringing reef growth and morphology: A review. *Earth-Science Reviews*, *57*(3–4), 255–277. [https://doi.org/10.1016/S0012-8252\(01\)00077-0](https://doi.org/10.1016/S0012-8252(01)00077-0)
- Khair, K., Tsokas, G. N., & Sawaf, T. (1997). Crustal structure of the northern Levant region: Multiple source Werner deconvolution estimates for Bouguer gravity anomalies. *Geophysical Journal International*, *128*(3), 605–616. <https://doi.org/10.1111/j.1365-246X.1997.tb05322.x>
- Khanna, P., Petrovic, A., Ramdani, A. I., Homewood, P., Mettraux, M., & Vahrenkamp, V. (2021). Mid-Holocene to present circum-Arabian sea level database: Investigating future coastal ocean inundation risk along the Arabian plate shorelines. *Quaternary Science Reviews*, *261*, 106959. <https://doi.org/10.1016/j.quascirev.2021.106959>
- Klinger, Y., Avouac, J. P., Dorbath, L., Karaki, N. A., & Tisnerat, N. (2000). Seismic behaviour of the Dead Sea fault along Araba Valley, Jordan. *Geophysical Journal International*, *142*(3), 769–782. <https://doi.org/10.1046/j.1365-246X.2000.00166.x>
- Lazar, B., Enmar, R., Schossberger, M., Bar-Matthews, M., Halicz, L., & Stein, M. (2004). Diagenetic effects on the distribution of uranium in live and Holocene corals from the Gulf of Aqaba. *Geochimica et Cosmochimica Acta*, *68*(22), 4583–4593. <https://doi.org/10.1016/j.gca.2004.03.029>
- Lazar, B., & Stein, M. (2011). Freshwater on the route of hominids out of Africa revealed by U-Th in Red Sea corals. *Geology*, *39*(11), 1067–1070. <https://doi.org/10.1130/G32257.1>
- Le Béon, M., Klinger, Y., Al-Qaryouti, M., Mériaux, A. S., Finkel, R. C., Elias, A., et al. (2010). Early holocene and late pleistocene slip rates of the southern Dead Sea fault determined from ^{10}Be cosmogenic dating of offset alluvial deposits. *Journal of Geophysical Research*, *115*(B11), 1–24. <https://doi.org/10.1029/2009JB007198>
- Le Béon, M., Klinger, Y., Amrat, A. Q., Agnon, A., Dorbath, L., Baer, G., et al. (2008). Slip rate and locking depth from GPS profiles across the southern Dead Sea Transform. *Journal of Geophysical Research*, *113*(B11), 1–19. <https://doi.org/10.1029/2007JB005280>
- Le Béon, M., Klinger, Y., Mériaux, A. S., Al-Qaryouti, M., Finkel, R. C., Mayyas, O., & Tapponnier, P. (2012). Quaternary morphotectonic mapping of the Wadi Araba and implications for the tectonic activity of the southern Dead Sea fault. *Tectonics*, *31*(5), 1–25. <https://doi.org/10.1029/2012TC003112>
- Lefevre, M. (2018). Segmentation des grands décrochements, du cycle seismique à la déformation long terme, exemple de la faille du Levant (p. 228).
- Le Pichon, X. T., & Gaulier, J.-M. (1988). The rotation of Arabia and the Levant fault system. *Tectonophysics*, *153*(1–4), 271–294. [https://doi.org/10.1016/0040-1951\(88\)90020-0](https://doi.org/10.1016/0040-1951(88)90020-0)
- Li, X., Jónsson, S., & Cao, Y. (2021). Interseismic deformation from Sentinel-1 Burst-overlap interferometry: Application to the Southern Dead Sea Fault. *Geophysical Research Letters*, *48*(16), 1–10. <https://doi.org/10.1029/2021GL093481>
- Lisiecki, L. E., & Raymo, M. E. (2005). A Pliocene-Pleistocene stack of 57 globally distributed benthic $\delta^{18}\text{O}$ records. *Paleoceanography*, *20*, 1–17. <https://doi.org/10.1029/2004PA001071>
- Lyberis, N. (1988). Tectonic evolution of the Gulf of Suez and the Gulf of Aqaba. *Tectonophysics*, *153*(1–4), 209–220. [https://doi.org/10.1016/0040-1951\(88\)90016-9](https://doi.org/10.1016/0040-1951(88)90016-9)
- Manaa, A. A. (2016). Late Pleistocene raised coral reefs along the Saudi Arabian Red Sea Coast.
- Manaa, A. A., Jones, B. G., McGregor, H. V., Zhao, J. X., & Price, D. M. (2016). Dating Quaternary raised coral terraces along the Saudi Arabian Red Sea coast. *Marine Geology*, *374*, 59–72. <https://doi.org/10.1016/j.margeo.2016.02.002>
- Mart, Y., & Ross, D. A. (1987). Post-Miocene rifting and diapirism in the northern Red Sea. *Marine Geology*, *74*(3–4), 173–190. [https://doi.org/10.1016/0025-3227\(87\)90049-1](https://doi.org/10.1016/0025-3227(87)90049-1)
- Martel, S. J., Stock, G. M., & Ito, G. (2014). Mechanics of relative and absolute displacements across normal faults, and implications for uplift and subsidence along the eastern escarpment of the Sierra Nevada, California. *Geosphere*, *10*(2), 243–263. <https://doi.org/10.1130/GES00968.1>
- Masson, F., Hamiel, Y., Agnon, A., Klinger, Y., & Deprez, A. (2015). Variable behavior of the Dead Sea Fault along the southern Arava segment from GPS measurements. *Comptes Rendus Geoscience*, *347*(4), 161–169. <https://doi.org/10.1016/j.crte.2014.11.001>
- Mergner, H., & Schuhmacher, H. (1974). Morphologie, Ökologie und Zonierung von Korallenriffen bei Aqaba, (Golf von Aqaba, Rotes Meer). *Helgoländer wissenschaftliche Meeresuntersuchungen*, *26*(3–4), 238–358. <https://doi.org/10.1007/bf01627619>
- Meschis, M., Roberts, G. P., Robertson, J., & Briant, R. M. (2018). The relationships between regional quaternary uplift, deformation across active normal faults, and historical seismicity in the upper plate of subduction zones: The Capo D'Orlando Fault, NE Sicily. *Tectonics*, *37*(5), 1231–1255. <https://doi.org/10.1029/2017TC004705>
- Meschis, M., Roberts, G. P., Robertson, J., Mildon, Z. K., Sahy, D., Goswami, R., et al. (2022). Out of phase Quaternary uplift-rate changes reveal normal fault interaction, implied by deformed marine palaeoshorelines. *Geomorphology*, *416*, 108432. <https://doi.org/10.1016/j.geomorph.2022.108432>

- Moustafa, Y. A., Pätzold, J., Loya, Y., & Wefer, G. (2000). Mid-Holocene stable isotope record of corals from the northern Red Sea. *International Journal of Earth Sciences*, 88(4), 742–751. <https://doi.org/10.1007/s005310050302>
- Niemi, T. M., Zhang, H. W., Atallah, M., & Harrison, J. B. J. (2001). Late Pleistocene and Holocene slip rate of the Northern Wadi Araba fault, Dead Sea Transform, Jordan. *Journal of Seismology*, 5(3), 449–474. <https://doi.org/10.1023/A:1011487912054>
- Ota, Y., Chappell, J., Kelley, R., Yonekura, N., Matsumoto, E., Nishimura, T., & Head, J. (1993). Holocene coral reef terraces and coseismic uplift of Huon Peninsula, Papua New Guinea. *Quaternary Research*, 40(2), 177–188. <https://doi.org/10.1006/qres.1993.1070>
- Parker, J. H., Gischler, E., & Eisenhauer, A. (2012). Biodiversity of foraminifera from Late Pleistocene to Holocene coral reefs, South Sinai, Egypt. *Marine Micropaleontology*, 86–87, 59–75. <https://doi.org/10.1016/j.marmicro.2012.02.002>
- Patton, T. L., Moustafa, A. R., Nelson, R. A., & Abdine, S. A. (1994). Tectonic evolution and structural setting of the Suez Rift: Interior rift basins (pp. 9–55). <https://doi.org/10.1306/m59582c2>
- Pedoja, K., Husson, L., Regard, V., Cobbold, P. R., Ostanciaux, E., Johnson, M. E., et al. (2011). Relative sea-level fall since the last interglacial stage: Are coasts uplifting worldwide? *Earth-Science Reviews*, 108(1–2), 1–15. <https://doi.org/10.1016/j.earscirev.2011.05.002>
- Pietrantonio, G., Devoti, R., Mahmoud, S., & Riguzzi, F. (2016). Kinematics of the Suez-Sinai area from combined GPS velocity field. *Journal of Geodynamics*, 102, 231–238. <https://doi.org/10.1016/j.jog.2016.10.003>
- Plaziat, J. C., Baltzer, F., Choukri, A., Conchon, O., Freydet, P., Orszag-Sperber, F., et al. (1998). Quaternary marine and continental sedimentation in the northern Red Sea and Gulf of Suez (Egyptian coast): Influences of rift tectonics, climatic changes and sea-level fluctuations. In *Sedimentation and tectonics in rift basins Red Sea-Gulf of Aden* (pp. 537–573). Springer.
- Plaziat, J. C., Reyss, J. L., Choukri, A., & Cazala, C. (2008). Diagenetic rejuvenation of raised coral reefs and precision of dating. The contribution of the Red Sea reefs to the question of reliability of the Uranium-series datings of middle to late Pleistocene key reef-terraces of the world. *Carnets de Géologie*, 04(Articles), 1–35. <https://doi.org/10.4267/204216743>
- Pons-Branchu, E., Douville, E., Roy-Barman, M., Dumont, E., Branchu, P., Thil, F., et al. (2014). A geochemical perspective on Parisian urban history based on U--Th dating, laminae counting and yttrium and REE concentrations of recent carbonates in underground aqueducts. *Quaternary Geochronology*, 24, 44–53. <https://doi.org/10.1016/j.quageo.2014.08.001>
- Reilinger, R., McClusky, S., & ArRajehi, A. (2015). Geodetic constraints on the geodynamic evolution of the Red Sea. In N. M. A. Rasul & I. C. F. Stewart (Eds.), *The Red Sea, Springer Earth System Sciences* (pp. 135–149). Springer Berlin Heidelberg. <https://doi.org/10.1007/978-3-662-45201-1>
- Ribot, M., Klinger, Y., Jónsson, S., Avsar, U., Pons-Branchu, E., Matrau, R., & Mallon, F. L. (2021). Active faults' geometry in the Gulf of Aqaba, Southern Dead Sea Fault, illuminated by Multibeam Bathymetric Data. *Tectonics*, 40(4), e2020TC006443. <https://doi.org/10.1029/2020TC006443>
- Ribot, M., Lefèvre, M., Klinger, Y., Pons-Branchu, E., Dapoigny, A., & Jonsson, S. (2024). Bathymetric data from the Northern Red Sea [Dataset]. *Zenodo*. <https://doi.org/10.5281/zenodo.11610050>
- Roberts, G. P., Houghton, S. L., Underwood, C., Papanikolaou, I., Cowie, P. A., Van Calsteren, P., et al. (2009). Localization of quaternary slip rates in an active rift in 105 years: An example from central Greece constrained by ²³⁴U-²³⁰Th coral dates from uplifted paleoshorelines. *Journal of Geophysical Research*, 114(B10), 1–26. <https://doi.org/10.1029/2008JB005818>
- Roberts, G. P., Meschis, M., Houghton, S., Underwood, C., & Briant, R. M. (2013). The implications of revised Quaternary palaeoshoreline chronologies for the rates of active extension and uplift in the upper plate of subduction zones. *Quaternary Science Reviews*, 78, 169–187. <https://doi.org/10.1016/j.quascirev.2013.08.006>
- Robinson, L. F., Belshaw, N. S., & Henderson, G. M. (2004). U and Th concentrations and isotope ratios in modern carbonates and waters from the Bahamas. *Geochimica et Cosmochimica Acta*, 68(8), 1777–1789. <https://doi.org/10.1016/j.gca.2003.10.005>
- Roeser, H. A. (1975). A detailed magnetic survey of the Southern Red Sea (pp. 143–165).
- Rohling, E. J., Grant, K., Bolshaw, M., Roberts, A. P., Siddall, M., Hemleben, C., & Kucera, M. (2009). Antarctic temperature and global sea level closely coupled over the past five glacial cycles. *Nature Geoscience*, 2(7), 500–504. <https://doi.org/10.1038/ngeo557>
- Rohling, E. J., Grant, K., Hemleben, C., Siddall, M., Hoogakker, B. A. A., Bolshaw, M., & Kucera, M. (2007). High rates of sea-level rise during the last interglacial period. *Nature Geoscience*, 1, 38–42. <https://doi.org/10.1038/ngeo.2007.28>
- Rohling, E. J., Medina-Elizalde, M., Shepherd, J. G., Siddall, M., & Stanford, J. D. (2012). Sea surface and high-latitude temperature sensitivity to radiative forcing of climate over several glacial cycles. *Journal of Climate*, 25(5), 1635–1656. <https://doi.org/10.1175/2011JCLI4078.1>
- Ryan, W. B. F., Carbotte, S. M., Coplan, J. O., O'Hara, S., Melkonian, A., Arko, R., et al. (2009). Global multi-resolution topography synthesis. *Geochemistry, Geophysics, Geosystems*, 10(3), Q03014. <https://doi.org/10.1029/2008GC002332>
- Sade, A. R., Hall, J. K., Tibor, G., Niemi, T. M., Ben-Avraham, Z., Al-Zoubi, A. A., et al. (2009). The multinational bathymetric survey: Northern Gulf of Aqaba/Elat Poster. *Israel Journal of Earth Sciences*, 57(2), 139–144. <https://doi.org/10.1560/IJES.57.2.139>
- Sadeh, M., Hamiel, Y., Ziv, A., Bock, Y., Fang, P., & Wdowinski, S. (2012). Crustal deformation along the Dead Sea Transform and the Carmel Fault inferred from 12 years of GPS measurements. *Journal of Geophysical Research*, 117(B8), 1–14. <https://doi.org/10.1029/2012JB009241>
- Schick, A. P. (1958). Terraces on Tiran Island, Northern Red Sea. *Geografiska Annaler*, 40(1), 63–66. <https://doi.org/10.1080/20014422.1958.11880924>
- Scholz, D., Mangini, A., & Felis, T. (2004). U-series dating of diagenetically altered fossil reef corals. *Earth and Planetary Science Letters*, 218(1–2), 163–178. [https://doi.org/10.1016/S0012-821X\(03\)00647-2](https://doi.org/10.1016/S0012-821X(03)00647-2)
- Shaked, Y., Agnon, A., Lazar, B., Marco, S., Avner, U., & Stein, M. (2004). Large earthquakes kill coral reefs at the north-west Gulf of Aqaba. *Terra Nova*, 16(3), 133–138. <https://doi.org/10.1111/j.1365-3121.2004.00541.x>
- Shaked, Y., Lazar, B., Marco, S., Stein, M., & Agnon, A. (2011). Late Holocene events that shaped the shoreline at the northern Gulf of Aqaba recorded by a buried fossil reef. *Israel Journal of Earth Sciences*, 58(3), 355–368. <https://doi.org/10.1560/IJES.58.3-4.355>
- Shaked, Y., Lazar, B., Marco, S., Stein, M., Tchermov, D., & Agnon, A. (2005). Evolution of fringing reefs: Space and time constraints from the Gulf of Aqaba. *Coral Reefs*, 24(1), 165–172. <https://doi.org/10.1007/s00338-004-0454-2>
- SHOM. (2004). Mission Océanographique de l'atlantique - Egypte, Abords de Sharm el-sheikh, rapport particulier 10 MOA/DR 24 Janvier 2004.
- Siddall, M., Bard, E., Rohling, E. J., & Hemleben, C. (2006). Sea-level reversal during termination II. *Geology*, 34(10), 817–820. <https://doi.org/10.1130/G22705.1>
- Siddall, M., Rohling, E., Almogi-Labin, A., Hemleben, C., Meischner, D., Schmelzer, I., & Smeed, D. A. (2003). Sea-level fluctuations during the last glacial cycle. *Nature*, 423(6942), 853–858. <https://doi.org/10.1038/nature01687.1>
- Taviani, M., Montagna, P., Rasul, N. M. A., Angeletti, L., & Bosworth, W. (2019). Pleistocene coral reef terraces on the Saudi Arabian side of the Gulf of Aqaba, Red Sea. In N. M. A. Rasul & I. C. F. Stewart (Eds.), *Geological setting, palaeoenvironment and archaeology of the Red Sea* (pp. 341–365). Springer International Publishing. <https://doi.org/10.1007/978-3-319-99408-6>
- Thompson, W. G., Spiegelman, M. W., Goldstein, S. L., & Speed, R. C. (2003). An open-system model for U-series age determinations of fossil corals. *Earth and Planetary Science Letters*, 210(1–2), 365–381. [https://doi.org/10.1016/S0012-821X\(03\)00121-3](https://doi.org/10.1016/S0012-821X(03)00121-3)

- Tissot, F. L. H., Chen, C., Go, B. M., Naziemiec, M., Healy, G., Bekker, A., et al. (2018). Controls of eustasy and diagenesis on the $^{238}\text{U}/^{235}\text{U}$ of carbonates and evolution of the seawater ($^{234}\text{U}/^{238}\text{U}$) during the last 1.4 Myr. *Geochimica et Cosmochimica Acta*, 242, 233–265. <https://doi.org/10.1016/j.gca.2018.08.022>
- Tubbs, R. E., Fouda, H. G. A., Afifi, A. M., Raterman, N. S., Hughes, G. W., & Fadolkarem, Y. K. (2014). Midyan Peninsula, northern Red Sea, Saudi Arabia: Seismic imaging and regional interpretation. *GeoArabia*, 19(3), 165–184. <https://doi.org/10.2113/geoarabia1903165>
- Viltres, R., Jónsson, S., Alothman, A. O., Liu, S., Leroy, S., Masson, F., et al. (2022). Present-day motion of the Arabian Plate. *Tectonics*, 41(3), 1–18. <https://doi.org/10.1029/2021TC007013>
- Wdowinski, S., Bock, Y., Baer, G., Prawirodirdjo, L., Bechor, N., Naaman, S., et al. (2004). GPS measurements of current crustal movements along the Dead Sea Fault. *Journal of Geophysical Research*, 109(B5), 1–16. <https://doi.org/10.1029/2003JB002640>
- Wechsler, N., Rockwell, T. K., & Klinger, Y. (2018). Variable slip-rate and slip-per-event on a plate boundary fault: The Dead Sea fault in northern Israel. *Tectonophysics*, 722, 210–226. <https://doi.org/10.1016/j.tecto.2017.10.017>
- Weil, N. (2008). *Holocene coral reefs evolution in the Gulf of Aqaba: Terraces, sea-levels and growth patterns*. Hebrew University.
- Woodroffe, C. D., McGregor, H. V., Lambeck, K., Smithers, S. G., & Fink, D. (2012). Mid-Pacific microatolls record sea-level stability over the past 5000 yr (pp. 951–955). <https://doi.org/10.1130/G33344.1>
- Woodroffe, C. D., & Webster, J. M. (2014). Coral reefs and sea-level change. *Marine Geology*, 352, 248–267. <https://doi.org/10.1016/j.margeo.2013.12.006>
- Yehudai, M., Lazar, B., Bar, N., Kiro, Y., Agnon, A., Shaked, Y., & Stein, M. (2017). U–Th dating of calcite corals from the Gulf of Aqaba. *Geochimica et Cosmochimica Acta*, 198, 285–298. <https://doi.org/10.1016/j.gca.2016.11.005>
- Yokoyama, Y., Esat, T. M., & Lambeck, K. (2001). Coupled climate and sea-level changes deduced from Huon Peninsula coral terraces of the last ice age. *Earth and Planetary Science Letters*, 193(3–4), 579–587. [https://doi.org/10.1016/s0012-821x\(01\)00515-5](https://doi.org/10.1016/s0012-821x(01)00515-5)

References From the Supporting Information

- Lowe, D. G. (2004). Distinctive image features from scale-invariant keypoints. *International Journal of Computer Vision*, 60(2), 91–110. <https://doi.org/10.1023/b:visi.0000029664.99615.94>
- Rosu, A.-M., Pierrot-Deseilligny, M., Delorme, A., Binet, R., & Klinger, Y. (2015). Measurement of ground displacement from optical satellite image correlation using the free open-source software MicMac. *ISPRS Journal of Photogrammetry and Remote Sensing*, 100, 48–59. <https://doi.org/10.1016/j.isprsjprs.2014.03.002>